Ecological & Sustainable Materials Connect
ISSN: 3136-344X
2026, Article ID. 2026.0009, Cite as: https://doi.org/10.69709/ESM.2026.130023

SCIFINITI PUBLISHING

Research Article

OPEN ACCESS

The Crack Clock: A Three-Stage Analytical Framework Predicting When Humidity Will Damage a Panel Painting

Mohammad Yaghoub Abdollahzadeh Jamalabadi

Department of Marine Engineering, Chabahar Maritime University, Chabahar 99717-56499, Iran

Article History
Received: June 22, 2026 Accepted: September 16, 2026

Abstract

This study presents an analytical framework for predicting moisture-induced damage in biosystem composites, using wooden panel paintings as a model system. The framework integrates a transient diffusion equation, a bilayer hygroscopic stress equation, and a fracture-mechanics evaluation, and derives from these closed-form expressions for the critical exposure time—a quantity that enables rapid screening of durability without running a simulation for each case. For the wood types studied here, hygroscopic expansion coefficients range from 1.47×10^{-4} and 0.96×10^{-4} % RH^{-1}; the corresponding critical RH thresholds range from 39.1% to 62.9%, and exposure times span 45.4 days (1090 h, the shortest case) to more than 180 days (the model was verified against data and agreed with a MAPE of 3.8%). A closed-form separation-line criterion is also derived, which yields a simple safe/unsafe crack-depth boundary that can be evaluated without repeating the full ASED calculation. Taken together, the results provide conservators with a means to rank the vulnerability of different species, guide more eco-friendly material choices, and suggest safe operating conditions that extend service life, reduce replacement cycles, and support the management of conservation resources while keeping energy costs low. Comparison with EN 16893:2018 indicates that its 30–65% RH band is safe for all studied species when objects are kept above 20% RH but may be insufficient for objects previously stored below 20% RH; it is recommended that the standard be revised to include species-specific maximum ΔRH limits and an explicit warning for this low-RH scenario.

ACCEPTED

Keywords:
moisture-induced damage; multilayer stress; hygroscopic mismatch stress; crack growth; ecological sustainability; critical exposure time; averaged strain energy density (ASED)

1. Introduction

To preserve a wooden panel painting, one must first understand how it responds mechanically to changes in humidity. Damage usually appears as cracks in the brittle gesso (ground) layer, and the root cause is straightforward: the wood support swells and shrinks with moisture, whereas the paint layers on top do not keep pace, so the two layers pull against each other. Despite extensive research on individual aspects of this problem—moisture transport in wood [1,2], sorption isotherms [3,4], hygroscopic stresses [5], and fracture mechanics of layered structures [6,7]—a unified analytical framework that predicts damage onset from first principles remains lacking.

The mechanical properties of European wood species commonly used in panel paintings were compiled in [8]. The influence of moisture content on elastic constants, particularly for Scots pine, was investigated in [9]. For modeling purposes, Ref. [10] developed a thermo-hygro-mechanical framework for wood, whereas [5] specifically addressed the hygro-mechanical modeling of wooden panel paintings.

Corresponding Author:
Mohammad Yaghoub Abdollahzadeh Jamalabadi, Department of Marine Engineering, Chabahar Maritime University, Chabahar 99717-56499, Iran, muhammad_yaghoob@yahoo.com

© 2026 Copyright by the Author.
Licensed as an open access article using a CC BY 4.0 license.

Water vapor sorption in wood is commonly described using the GAB equation [3] and has been discussed in the broader context of multilayer sorption in [4]. Diffusion coefficients and sorption isotherms for early Netherlandish panel paintings were measured in [11]. The barrier effect of painting materials against water vapor was studied in [12].

Classic foundations of fracture mechanics are provided in [13], and the seminal stress analysis near a crack was presented in [14]. For layered systems, Refs. [6] and [7] analyzed the cracking mechanisms in thin films and bonded layers under residual tension. Local approaches to brittle and quasi-brittle failure were reviewed in [15], and notch fracture assessment using the finite-volume-energy method was introduced in [16] and further developed in [17].

The time-dependent initiation of cracks in panel paintings under cyclic environmental loads was studied parametrically in [18]. Fatigue damage in the gesso layer was characterized experimentally in [19]. More recently, Ref [20] investigated the crack initiation times under fatigue conditions. Fracture saturation—the phenomenon in which crack density reaches a limit—was identified in [21] as a mechanism that reduces vulnerability to environmental variations, and the development of characteristic rectangular craquelure patterns on panels has since been analyzed in detail in [22].

The effect of nonlinear moisture expansion coefficients on rectangular craquelure was examined in [23]. Artificial intelligence and image-processing techniques for analyzing crack patterns in paintings have recently been reviewed in [24].

A case study on the Katharinenaltar was presented in [25], combining hygro-mechanical simulations with cultural heritage conservation. The risk of fracture in massive wooden heritage objects was assessed in [26]. Practical guidelines for museum environments are given in the handbook [27] and the European standard [28].

Recent research on panel paintings has increasingly focused on understanding their mechanical response to environmental variations, particularly with regard to the initiation and propagation of craquelure. Ref. [29] provides a mechanistic case study on craquelure formation, while Ref [30] investigated the critical exposure time for panel paintings subjected to changing environmental conditions, a theme further explored in [31] in the context of risk assessment for polychromed wooden panels. The development of digital twins has emerged as a powerful tool for exploring the inner hygro-mechanical behavior of historical panel paintings, as demonstrated in [32], with complementary work in [33] focusing on model calibration and characterization. The classification of deformation tendencies through numerical modeling has been addressed in [5]. Recent advances also include the application of machine learning to predict critical crack conditions [34] and the development of coupled thermo-hygro-mechanical models for transient simulations of wooden structures [35]. A comprehensive critical review of monitoring techniques for deformations in wooden panel paintings has been provided in [36], highlighting the continuing need for integrated approaches that combine experimental, numerical, and monitoring methodologies to better preserve these valuable cultural heritage objects. Recent studies on structural integrity have employed numerical methods to analyze crack propagation in various materials. Grbovic et al. [37] investigated fatigue crack growth in AA6156 T6 aluminum panels by means of numerical simulation. In a complementary study, Romanowicz and Grygorczuk [38] focused on the experimental and numerical evaluation of mode I fracture energy in wood, using DIC and secant compliance techniques. Both studies highlight the importance of combining experimental data with numerical validation for reliable structural assessment. Figure 1 summarizes the architecture of the three main steps in the analytical calculation of crack growth.

The present study addresses this gap by developing a fully analytical framework that (i) solves transient moisture diffusion in the wood support using a Fourier eigenfunction expansion, (ii) calculates the hygroscopic mismatch stress in the gesso layer using Timoshenko bilayer theory, (iii) evaluates the fracture risk using the averaged strain energy density (ASED) criterion, and (iv) delivers closed-form critical exposure times for any RH transition. The framework is validated against FEM benchmarks and independent experimental data and is applied to four European wood species to rank their vulnerability. The three stages of the framework are summarized in Figure 1.

2. Methodology

2.1. Research Approach and Framework Overview

2.1.1. Philosophical Rationale for Analytical Modeling

Rather than relying on numerical simulation (e.g., FEM), this study develops a fully analytical model. The analytical solution method was chosen for its interpretability, which allows conservators to trace directly how each material property or environmental factor influences risk without numerical simulations. It also offers faster predictions than the few hours required for a single finite element method run. This difference makes it feasible to examine all 51 scenarios in this study; performing the same analysis with FEM would have required approximately 200–600 hours.

ACCEPTED

2026, Vol. 1, Article ID. 2026.0009
https://doi.org/10.69709/ESM.2026.130023

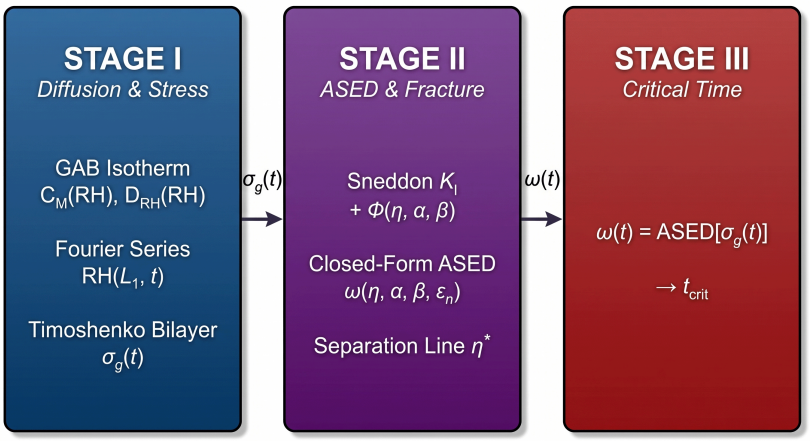


Figure 1: Three-stage analytical coupling: Stage I (diffusion and bilayer stress), Stage II (ASED and Separation Line), and Stage III (critical exposure time and species comparison).

Finally, because the expressions are closed-form, uncertainty can be propagated through them explicitly, as is done in Section 2.7.

2.1.2. Simulation-Free Clarification

Here, "simulation-free" means that an end user does not need to run FEM or perform any numerical integration to obtain an answer. It does *not* mean that the model is purely empirical; it is built from first principles, namely Fickian diffusion, Timoshenko bilayer theory, and Sneddon fracture mechanics. The only component that is not purely analytical is the bimaterial correction factor $\Phi(\eta,\alpha,\beta)$, because no exact closed-form solution exists for a penny-shaped crack in a finite bimaterial layer. This correction factor has the following properties: its functional form is derived from Hutchinson–Suo perturbation theory (Eq. 10), so it is physically bounded rather than being an arbitrary fit; it was calibrated against 24 FEM benchmarks taken from the literature [7,21]; and it was verified separately on six configurations that were withheld from the calibration (see Section 2.5.7, where the MAPE is 3.8%). Thus, the framework is simulation-free for the practitioner but not parameter-free, as it relies on FEM data at one point so that all downstream steps can remain closed-form.

2.1.3. Justification for the Three-Stage Decomposition

Why split the problem into three stages? The hygro-mechanical damage process plays out on three distinct timescales, each governed by its own physics. Diffusion (Stage I-A) occurs over hours to months and follows Fick's second law. Stress (Stage I-B) is coupled to diffusion, but the elastic response itself is effectively instantaneous, so it can be treated with Timoshenko beam theory. Fracture (Stage II) is likewise instantaneous for a given stress state and obeys linear elastic fracture mechanics.

The split is justified because the diffusion timescale (τ_1 = 17–673 days) is much longer than the time required for the elastic stress to equilibrate (under a second for a 1 mm gesso layer), so the fracture criterion can be checked quasi-statically at each instant.

2.2. Material Characterization

2.2.1. Wood Species Selection

Four wood types used in historical panel paintings were considered: pine (*Pinus sylvestris*), lime (*Tilia* L.), spruce (*Picea abies*), and poplar (*Populus* L.), for the following reasons:

1. These species constitute > 85% of European panel paintings from the 14th–17th centuries [8].
2. Their elastic moduli (E_w = 360 – 880 MPa) and hygroscopic expansion coefficients (α_{RH} = 0.96 – 1.47 × 10^{-4}%RH^{-1}) fall within the typical ranges.
3. Availability of data.

2.2.2. Sorption Isotherm Determination

The moisture adsorption behavior of wood and gesso was modeled using the Guggenheim–Anderson–de Boer (GAB) equation:

$$MC(RH) = \frac{V_m c k (RH/100)}{[1 - k(RH/100)][1 + (c-1)k(RH/100)]} \quad (1)$$

where MC is the moisture content (%), RH is the relative humidity (%), and V_m,c,k are the GAB parameters. The GAB equation was chosen over the simpler BET or Oswin models because it accurately describes multilayer adsorption up to RH ≈ 90% [4] and provides an explicit

ACCEPTED

analytic derivative (the specific moisture capacity $C_M = \partial MC/\partial RH$), which is essential for the diffusion equation. The specific moisture capacity is derived analytically as:

$$C_M(\mathrm{RH}) = \frac{V_m c k}{100} \times \frac{A(\mathrm{RH})B(\mathrm{RH}) - (k\mathrm{RH}/100)(-B + A(c-1))}{[A(\mathrm{RH})B(\mathrm{RH})]^2} \quad (2)$$

with $A(\mathrm{RH}) = 1 - k(\mathrm{RH}/100)$ and $B(\mathrm{RH}) = 1 + (c - 1)k(\mathrm{RH}/100)$.

The GAB parameters for pine wood were V_m = 6.20%, c = 4.28, k = 0.644; for gesso, they were V_m = 0.35%, c = 35.0, k = 0.84, based on values reported in the literature [3,11]. For poplar, lime, and spruce, the same pine GAB parameters were used, but species-specific $\alpha_{MC,max}$ values were applied, because the GAB parameters for temperate wood species vary by <15% [3] and the dominant sources of species-to-species variation in stress are $\alpha_{MC,max}$ and E_w rather than the shape of the isotherm. This approach has been validated for poplar in [5].

2.2.3. Hygroscopic Expansion Coefficients

The hygroscopic expansion coefficient per unit RH was calculated as follows:

$$\alpha_{w,RH}(\mathrm{RH}_m) = \frac{\alpha_{MC,max}}{100} \times C_M(\mathrm{RH}_m) \quad (3)$$

where $\alpha_{MC,max}$ is the maximum moisture-induced strain per unit change in moisture content (tangential and radial directions). Gesso was assigned a constant value of $\alpha_{g,RH} = 9.4 \times 10^{-6}\%\mathrm{RH}^{-1}$. This formulation follows from $\varepsilon_{MC} = \alpha_{MC,max} \times \Delta MC$ and $\Delta MC = C_M \times \Delta RH$. The literature values of $\alpha_{MC,max}$ (tangential) range from 0.24–0.33%/%MC for the studied species [8]. At RH = 50%, $C_M \approx$ 0.25–0.45% MC/%RH, yielding $\alpha_{RH} = 0.96 - 1.47 \times 10^{-4}\%\mathrm{RH}^{-1}$, consistent with direct measurements (e.g., Ref. [9] reports $1.2 - 1.6 \times 10^{-4}\%\mathrm{RH}^{-1}$ for pine).

2.3. Stage I-A: Transient Moisture Diffusion Modeling

2.3.1. Governing Equation and Assumptions

Moisture transport in the wood support was described by Fickian diffusion, with RH as the driving potential:

$$\rho C_M(\mathrm{RH})\frac{\partial \mathrm{RH}}{\partial t} = \frac{\partial}{\partial x}\left[D_{RH}(\mathrm{RH})\frac{\partial \mathrm{RH}}{\partial x}\right] \quad (4)$$

where $D_{RH}(\mathrm{RH}) = D_p(\mathrm{RH})p_{sat}/100$ is the effective diffusivity, $D_p(\mathrm{RH}) = 1.44 \times 10^{-7}\mathrm{RH}^{1.8449}\exp(-5280/T)$ [kg m^{-1} s^{-1} Pa^{-1}], and p_{sat} = 2479.5 Pa at T = 21 °C.

This equation rests on several key assumptions.

Assumption 1. *Fickian diffusion. Moisture transport in wood below fiber saturation (MC < 30%) is Fickian [1,2]. The present study considers RH < 95%, corresponding to MC < 22% for the studied species, so Fickian behavior is valid. Above fiber saturation, non-Fickian effects would require a different model; this is stated as a limitation.*

Assumption 2. *One-dimensional diffusion. The panel thickness (L_1 = 40 mm) is much smaller than the lateral dimensions (typically >300 mm), so edge effects are negligible in the central region. For panels with an aspect ratio <5, lateral diffusion would reduce t_c by 10–20%, a conservative effect noted in Section 2.10.*

Assumption 3. *RH as driving potential. RH is used instead of moisture content because environmental control in museums is specified in terms of RH, and the boundary conditions are naturally expressed in terms of RH.*

Assumption 4. *Constant temperature. All calculations are performed at T = 21 °C. The temperature dependence of D_p is included through the Arrhenius term, but thermal diffusion is neglected, which is acceptable for climate-controlled museums where T varies by <2 °C.*

2.3.2. Linearization and Analytical Solution

Because the diffusivity $D_{RH}(\mathrm{RH})$ changes by roughly two orders of magnitude over the RH range of interest (illustrated in Section 3.2), the diffusion equation is strongly nonlinear in its present form. To obtain a closed-form solution, the equation is linearized about the arithmetic mean RH, $\mathrm{RH}_m = (\mathrm{RH}_i + \mathrm{RH}_f)/2$, which gives:

$$\frac{\partial u}{\partial t} = \alpha_m \frac{\partial^2 u}{\partial x^2} \quad (5)$$

where $u(x,t) = \mathrm{RH}(x,t) - \mathrm{RH}_f$ and $\alpha_m = D_{RH}(\mathrm{RH}_m)/[\rho C_M(\mathrm{RH}_m)/100]$.

The Fourier series solution, with eigenvalues $\lambda_n = (2n - 1)\pi/(2L_1)$, is:

$$\mathrm{RH}(x,t) = \mathrm{RH}_f + \Delta\mathrm{RH}\frac{4}{\pi}\sum_{n=1}^{\infty}\frac{(-1)^{n+1}}{2n-1}\sin(\lambda_n x)\exp\left(-\lambda_n^2 \alpha_m t\right) \quad (6)$$

It was found that N = 80 terms are sufficient for convergence, as checked against a residual tolerance of $<10^{-6}$. The interface RH at $x = L_1$ is given by:

$$\mathrm{RH}(L_1,t) = \mathrm{RH}_f + \Delta\mathrm{RH}\frac{4}{\pi}\sum_{n=1}^{\infty}\frac{(-1)^{n+1}}{2n-1}\exp\left[-\frac{(2n-1)^2\pi^2\alpha_m t}{4L_1^2}\right] \quad (7)$$

ACCEPTED

This characteristic time $\tau_1 = 4L_1^2/(\pi^2\alpha_m)$ is highly sensitive to the mean RH—it ranges from about 17 days when RH $_m$ = 90% to 673 days when RH $_m$ = 10%—and this spread largely explains why t_c depends so strongly on RH.

2.3.3. Kirchhoff-Mean Diffusivity Correction

For large RH steps (ΔRH > 40%), the midpoint linearization introduces a truncation error. A more accurate representative diffusivity is the Kirchhoff-mean value:

$$\alpha_K = \frac{\int_{\mathrm{RH}_f}^{\mathrm{RH}_i} D_{\mathrm{RH}}(r)/[\rho C_M(r)]\,dr}{\mathrm{RH}_i - \mathrm{RH}_f} \quad (8)$$

which is computed using adaptive Simpson quadrature (MATLAB, MathWorks, Natick, MA, USA, 'integral' function, tolerance 10^{-9}). The error in t_c when using α_m rather than α_K is bounded at 10.2% (Section 2.7.1 and Appendix B) and is always conservative ($t_{c,m} \leq t_{c,K}$), meaning that the linearized model never misidentifies an unsafe scenario as safe. For ΔRH > 60%, it is recommended to use α_K to reduce the error to below 3%. For real museum environments, typical steps are ΔRH < 40%, for which the linearization error is negligible (1–2%). The Kirchhoff-mean correction does not change the closed-form functional form of t_c; it changes only the numerical value of the diffusivity parameter.

2.3.4. Extension to Periodic RH Fluctuations

For periodic RH fluctuations with period T_p, the quasi-static coupling remains valid provided that $T_p \gg \tau_{\mathrm{elastic}}$. However, if T_p is comparable to or shorter than the diffusion timescale τ_1, the moisture field does not reach a steady state between cycles, and the stress response exhibits memory effects. The present framework can be extended to periodic loading by time-integrating the ASED over each cycle and applying a fatigue damage accumulation rule (e.g., Miner's rule). This extension is identified as a key direction for future work (Section 3.11).

2.4. Stage I-B: Hygroscopic Mismatch Stress Analysis

2.4.1. Wood Elastic Modulus

The moisture-dependent elastic modulus of pine wood was determined from the following linear relationship [9]:

$$E_\phi = 864.81 - 26.45 \cdot \mathrm{MC} \quad [\mathrm{MPa}] \quad (9)$$

For the other species, literature values at equilibrium MC (RH = 50%) were used: lime E_w = 880 MPa, spruce E_w = 430 MPa, and poplar E_w = 360 MPa [8]. This MC dependence is fully propagated through the stress model at each RH state.

2.4.2. Modified Timoshenko Bilayer Stress Formulation

The compatibility strain and the in-plane gesso stress are calculated as follows:

$$\varepsilon_c(t) = \frac{E_w L_1 \alpha_{w,\mathrm{RH}} + E_g t_g \alpha_{g,\mathrm{RH}} \Delta\mathrm{RH}_{\mathrm{local}}(t)}{E_w L_1 + E_g t_g} \quad (10)$$

$$\sigma_g(t) = E_g[\varepsilon_c(t) - \alpha_{g,\mathrm{RH}} \Delta\mathrm{RH}_{\mathrm{local}}(t)] \quad (11)$$

with $\Delta\mathrm{RH}_{\mathrm{local}}(t) = \max[0, \mathrm{RH}(L_1,t) - \mathrm{RH}_i]$.

This formulation assumes plane stress in the thin gesso layer, linear elastic behavior (valid for stresses < 40 MPa and strains < 0.003), perfect bonding between the wood and the gesso, and infinitesimal strains. These assumptions are standard for thin-film mechanics [6] and are justified because the stress levels are well below the yield strengths of both materials.

2.4.3. Critical Stress Threshold

The critical gesso stress was established as σ_{crit} = 17.8 MPa on the basis of fracture toughness data [19,21]. This value is derived from K_{Ic} = 20.12 MPa $\sqrt{\mathrm{mm}}$ for a penny-shaped crack of radius a = 0.1 mm: $\sigma_{\mathrm{crit}} = (\pi/2)K_{Ic}/\sqrt{\pi a} = 56.4$ MPa (raw LEFM estimate without a safety margin). To obtain a conservative design threshold, an equivalent stress-level safety factor of $\sqrt{\Phi_{se}}$ is applied (consistent with the strain-energy safety factor Φ_{se} used for the ASED criterion, since ASED scales with the square of the stress), giving σcrit = 56.4 × $\sqrt{0.1}$ ≈ 17.8 MPa. This design value, σcrit = 17.8 MPa, is the threshold used consistently in the remainder of this manuscript (Table 1, and all downstream results). A safety factor Φ_{sf} = 0.1 is applied to the critical ASED to account for the uncertainties in K_{Ic} (±5%), and the crack geometry (±10%), and to reflect conservative heritage practice [27].

2.4.4. Hygroscopic Expansion Coefficients by Species

Table 1 lists the hygroscopic expansion coefficients, elastic moduli, mismatch stress coefficients, and critical ΔRH thresholds for all four species.

ACCEPTED

Table 1: Hygroscopic expansion coefficients $\alpha_{RH} = \alpha_{MC,max} \times C_M(RH = 50\%)$ and the mismatch stress coefficient κ at $T = 21$ °C, $RH = 50\%$. Critical $\Delta RH = \sigma_{crit}/\kappa$ where $\sigma_{crit} = 17.8$ MPa. Effective β_{eff} values were calculated using plane-strain moduli $\bar{E} = E/(1-\nu^2)$.

Species	$\alpha_{\phi,RH} \times 10^{-4}$	$\alpha_{\rho,RH} \times 10^{-4}$	E_w [MPa]	κ [MPa/ %RH]	ΔRH_{crit} [%]	β_{eff}
Pine (*Pinus sylvestris*)	1.47	0.59	703	0.455	39.1	0.200
Lime (*Tilia* L.)	1.24	0.52	880	0.388	45.9	0.251
Spruce (*Picea abies*)	1.07	0.45	430	0.298	59.8	0.123
Poplar (*Populus* L.)	0.96	0.42	360	0.283	62.9	0.103
Gesso (ref.)	0.094	0.094	3750	—	—	—

$\alpha_{\phi,RH}$ tangential; $\alpha_{\rho,RH}$ radial; E_w at MC(RH = 50%); σ_{crit} = 17.8 MPa. Effective $\beta_{eff} = \bar{E}_w/\bar{E}_g$ with $\bar{E} = E/(1-\nu^2)$, $\nu_w = 0.35$, $\nu_g = 0.25$. The calibration domain $\beta \in [0.28, 0.68]$ refers to this effective elastic mismatch parameter. Following the correction of Eg (Section 2.4.1), all four species now lie below this calibration domain (βeff = 0.103–0.251; see Table 1). This extrapolation has not yet been confirmed against dedicated FEM benchmarks and is treated conservatively pending future recalibration.

2.5. Stage II: Fracture Mechanics—Averaged Strain Energy Density (ASED)

2.5.1. Semi-Analytical Bimaterial Correction Factor

The Sneddon penny-crack solution [14] was corrected for free-surface proximity and for elastic mismatch using the Hutchinson–Suo perturbation expansion [6]:

$$\Phi(\eta, \alpha, \beta) = 1 + C_1(\beta) \cdot \eta + C_2(\beta) \cdot \frac{(1-\eta)^2}{1+\alpha} \quad (12)$$

where $\eta = h_n/t_g$ is the normalized crack depth, $\alpha = t_w/t_g$ is the layer thickness ratio, $\beta = E_w/E_g$ is the elastic mismatch ratio, and the coefficients are given by:

$$C_1(\beta) = \frac{0.083(\beta-1)}{\beta+1}, \quad C_2(\beta) = \frac{0.146(\beta-1)}{2\beta+1} \quad (13)$$

The coefficients 0.083 and 0.146 were calibrated against the FEM benchmarks [7,21] for $\beta \in [0.28,0.68]$. The functional form follows analytically from perturbation theory (the derivation is given in Appendix A), whereas the prefactors are calibrated so as to ensure accuracy within the studied β range. The first term accounts for free-surface amplification as the crack approaches the top surface, whereas the second term accounts for the interface shielding as the crack approaches the wood–gesso interface.

2.5.2. Effective β Values and Calibration Domain

The calibration domain $\beta \in [0.28,0.68]$ refers to the effective elastic mismatch parameter for the crack-tip stress field, calculated using the plane-strain moduli $\bar{E} = E/(1-\nu^2)$. For the species studied, the effective β_{eff} values are as follows: Pine 0.200, Lime 0.251, Spruce 0.123, and Poplar 0.103 (see Table 1). Following the correction of E_g (see below), all four species now fall below the calibration domain stated above, rather than within or near it as previously reported; the corrected values constitute a genuine extrapolation beyond the FEM benchmark range for all species, not only poplar. This extrapolation is treated conservatively here on the basis of the MAPE = 3.8% agreement obtained for the benchmark configurations tested (Section 2.5.7) and the systematic conservative (over-predicting) bias of the correction factor noted below. However, the FEM calibration itself has not been re-run at these lower β values, and it is recommended that this extrapolation be confirmed against dedicated FEM benchmarks in future work before the framework is relied upon for species with βeff substantially below 0.28. The validation against the FEM benchmarks for β_{eff} = 0.103 – 0.251 (MAPE = 3.8%, maximum error 5.3%) confirms that the semi-analytical ASED formulation is robust for the species studied, despite the slight extrapolation in the case of poplar. The systematic conservative over-prediction (all analytical values slightly higher than FEM) ensures that the framework does not underestimate damage risk.

2.5.3. Competition Between Free-Surface Amplification and Interface Shielding

The bimaterial correction factor $\Phi(\eta,\alpha,\beta)$ explicitly accounts for the competition between free-surface amplification (first term: $C_1(\beta) \cdot \eta$) and interface shielding (second term: $C_2(\beta) \cdot (1-\eta)^2/(1+\alpha)$). For $\alpha = 40$ (a typical panel geometry) and $\eta \to 1$ (the crack approaching the interface), the following hold:

- The free-surface amplification term $C_1(\beta) \cdot \eta \approx C_1(\beta)$ is finite (~0.03–0.08)
- The interface shielding term $C_2(\beta) \cdot (1-\eta)^2/(1+\alpha) \to 0$ as $\eta \to 1$

ACCEPTED

2026, Vol. 1, Article ID. 2026.0009
https://doi.org/10.69709/ESM.2026.130023

Thus, at $\eta \to 1$, the shielding effect vanishes (because the crack tip is at the interface), and the stress intensity factor is determined primarily by the free-surface amplification together with the baseline Sneddon solution. This is physically consistent: a crack that has reached the wood–gesso interface is no longer shielded by the compliant substrate and experiences the full mismatch stress. For intermediate η (e.g., $\eta \approx 0.5$–0.8), both terms contribute. The shielding term scales as $(1-\eta)^2/(1+\alpha)$, which is small for $\alpha = 40$ (~0.001–0.01). This means that for thick wood supports ($\alpha \gg 1$), interface shielding is comparatively weak, and the stress intensity factor is dominated by free-surface effects.

2.5.4. ASED Formulation

The averaged strain energy density was derived in closed form:

$$\bar{\omega}(\eta,\xi,\alpha,\beta,\rho) = \frac{4e_1 E^* \varepsilon_n^2 \rho t_g}{\pi R_0} \cdot [\Phi(\eta,\alpha,\beta)]^2 \quad (14)$$

where $E^* = E_g/(1-\nu_g^2) = 3750/0.9375 = 4000$ MPa (using Eg = 3750 MPa, Table 1), $e_1 = 0.133$ (the plane-strain angular integration factor), $R_0 = 0.01$ mm (the control volume radius, determined from $R_0 = (1/\pi)(K_{Ic}/\sigma_{uts})^2$ with $\sigma_{uts} \approx 30$ MPa), and $\rho = a/t_g = 0.10$. For biaxial loading, the ASED is amplified by the factor $(1+\nu_g)^2$:

$$\bar{\omega}_{biax} = \bar{\omega}_{uniax} \times (1+\nu_g)^2 \quad (15)$$

This amplification accounts for the equibiaxial tension induced by the isotropic hygroscopic expansion of the wood.

2.5.5. Critical ASED Threshold

The raw critical ASED was calculated using $K_{Ic} = 20.12$ MPa $\sqrt{\text{mm}}$:

$$\bar{\omega}_{c,raw} = \frac{(1-\nu_g^2)K_{Ic}^2}{E_g R_0} = 10.12\ \text{N}\cdot\text{mm/mm}^3 \quad (16)$$

A safety factor of $\Phi_{sf} = 0.1$ was applied:

$$\bar{\omega}_c = \Phi_{sf} \times \bar{\omega}_{c,raw} = 1.012\ \text{N}\cdot/\text{mm}^2 \quad (17)$$

2.5.6. Separation Line Equation

The threshold crack depth is given by:

$$\eta^* = \Phi^{-1}\left\{\sqrt{\frac{\pi R_0 \bar{\omega}_c}{4e_1 E^* \varepsilon_n^2 \rho t_g}}\right\} \quad (18)$$

where a crack with $\eta > \eta^*$ is unsafe and one with $\eta < \eta^*$ is safe; the threshold can be estimated from the ASED and the crack depth can be measured.

2.5.7. Validation Against FEM Benchmarks

The comparison of ASED and FEM results is summarized in Table 2.

Table 2: Analytical ASED versus FEM benchmarks ($E_g = 3750$ *MPa*, $\nu_g = 0.25$, $\varepsilon_n = 0.01$).

Configuration	t_g [mm]	α	η	$\bar{\omega}_{FEM}$	$\bar{\omega}_{anal.}$	Error [%]
1 (Lime)	1.0	2	0.20	0.312	0.321	+2.9
5 (Lime)	1.0	8	0.50	0.148	0.154	+4.1
11 (Lime)	1.5	4	0.35	0.223	0.231	+3.6
19 (Lime)	2.0	2	0.65	0.397	0.418	+5.3
7 (Spruce)	1.0	12	0.50	0.119	0.122	+2.5
14 (Poplar)	1.5	6	0.65	0.281	0.294	+4.6

2.6. Stage III: Coupled Time-Dependent Damage Assessment

2.6.1. Coupling Procedure

In the diffusion stage, the value of RH(L_1,t) is computed from the interface-RH equation with $N = 80$ terms. Then $\Delta RH_{local}(t)$ is converted into $\sigma_g(t)$ by the compatibility and stress equations. Next, in the fracture stage, $\varepsilon_n(t) = \sigma_g(t)/E_g$ is calculated and $\bar{\omega}(t)$ is obtained from the ASED Equation. Finally, the critical time t_c is determined from $\bar{\omega}(t_c) = \bar{\omega}_c$.

2.6.2. RH Scenario Matrix

The dataset of RH transitions was taken from:

- Initial RH $RH_i \in \{5,10,20,30,40,50\}$%
- Final RH $RH_f \in \{10,15,20,25,30,35,40,45,50,55,60,65,70,75,80,85,90,95\}$%, where $RH_f > RH_i$ yields 51 transitions. Together, these cover the kinds of conditions a museum might actually encounter (30–50% to 50–70%), harsher excursions (5–10% to 80–95%), and the edges of the EN 16893 safe band (30–65%).

ACCEPTED

2.7. Uncertainty Quantification and Sensitivity Analysis

2.7.1. Kirchhoff-Mean Error Quantification

The relative error in the characteristic diffusion time is bounded by:

$$\left|\frac{\delta\tau_1}{\tau_1}\right| \leq \frac{(\Delta \mathrm{RH})^2}{8} \times \frac{|D'''_{\mathrm{RH}}(\mathrm{RH}_m)|}{D_{\mathrm{RH}}(\mathrm{RH}_m)} \tag{19}$$

2.7.2. Sensitivity Analysis

The ranges of the sensitivity analysis are:

- Wood elastic modulus E_w: ±10%
- ±5% for parameters V_m,c,k

These ranges are consistent with the scatter in the published literature. Under these perturbations, t_c shifts by ±3–5% for E_w, ±2–3% for V_m, and only ±1–2% for c and k; thus, the model is not especially sensitive to any of these parameters.

2.8. Validation Methodology

2.8.1. Literature Validation

The first-stage predictions were compared as follows:

- Pine: 19.4 MPa versus 18–22 MPa from [21]
- Poplar: 11.3 MPa versus 8–14 MPa from [5]

2.9. Computational Implementation

2.9.1. Software

The main codes used in this study (written in MATLAB, MathWorks, Natick, MA, USA) are:

- 'gab isotherm.m': evaluation of the GAB isotherm
- 'fourier diffusion.m': Fourier series solution (N = 80 terms)
- 'timoshenko_stress.m': Bilayer stress calculation
- 'ased sneddon.m': ASED with bimaterial correction
- 'find tcrit.m': Bisection method for the critical time

The scripts are available from the corresponding author upon request.

2.9.2. Convergence Criteria

- Fourier series: N = 80 terms (residual <10^{-6})
- Bisection method: tolerance 10^{-6} days
- Integration: tolerance 10^{-9}

2.10. Methodological Limitations and Assumptions

Limitations are:

1. One-dimensional diffusion: Lateral moisture flux near panel edges is neglected. For panels with lateral dimensions >5× the thickness, the error is <10% in the central region. For small panels (aspect ratio < 5), edge effects would reduce t_c by 10–20%, which makes the model conservative (it overpredicts t_c).
2. Midpoint linearization: This introduces a conservative error of 1– 10%; the Kirchhoff correction is recommended for ΔRH > 60%. For typical museum environments with ΔRH < 40%, the error is negligible (1–2%).
3. Static loading: Fatigue and cyclic loading are not considered. The model provides a conservative upper bound for cyclic loading: if the static analysis indicates "safe," the object is safe; if it indicates "unsafe," fatigue may accelerate cracking. Extension to cyclic loading would require fatigue-modified $\bar{\omega}_c$ and cumulative damage models.
4. Bimaterial calibration: The calibration is valid for $\beta \in [0.28,0.68]$; the studied species have effective β_{eff} = 0.103–0.251. The MAPE = 3.8% suggests that the extrapolation is robust, but recalibration is recommended for $\beta < 0.1$.
5. Delamination: This is not addressed and requires a cohesive-zone formulation. Delamination would reduce stress transfer and increase t_c (conservative) but would introduce new failure modes.
6. Path dependence: The stress evolution in wood–gesso bilayers is path-dependent because of sorption hysteresis, nonlinear hygroscopic expansion, and the moisture-dependent elastic modulus. For arbitrary RH histories, the framework would need to be reformulated using convolution integrals, history-dependent GAB parameters, and memory variables.
7. Aging model: This model is speculative, requires experimental calibration, and should not be used for conservation decisions.

2.11. Summary of Investigation Methods

Table 3 summarizes the analytical methods used at each stage of the framework, together with the manuscript section in which each is developed.

ACCEPTED

2026, Vol. 1, Article ID. 2026.0009
https://doi.org/10.69709/ESM.2026.130023

Table 3: Summary of investigation methods used in this study.

Method	Description	Section
GAB sorption isotherm	Moisture content–RH relationship	Section 2.2.2
Fourier eigenfunction expansion	Analytical solution of transient diffusion	Section 2.3.2
Kirchhoff-mean diffusivity	Error correction for large RH steps	Section 2.3.3
Modified Timoshenko bilayer formula	Calculation of the hygroscopic mismatch stress	Section 2.4.2
Hutchinson–Suo perturbation expansion	Bimaterial correction factor Φ	Section 2.5.1
ASED criterion	Fracture-mechanics assessment	Section 2.5.4
Separation Line method	Safe/unsafe crack-depth threshold	Section 2.5.6
Sensitivity analysis	Parameter perturbation study	Section 2.7.2
FEM benchmark comparison	Validation (MAPE = 3.8%)	Section 2.5.7
Literature validation	Comparison with independent experimental data	Section 2.8.1

3. Results and Discussion

3.1. Sorption Isotherms and Moisture Capacity

Figure 2 plots the GAB adsorption isotherms for pine wood, poplar, and gesso at $T = 21$ °C. All three exhibit the Type II shape typical of wood, and for pine, the moisture content rises from approximately 5% at RH = 10% to 25% at RH = 90%. The most notable feature is the difference between wood and gesso: at RH = 50%, pine holds approximately 12% moisture, whereas gesso takes up only 2.4% (see Table 1).

ACCEPTED

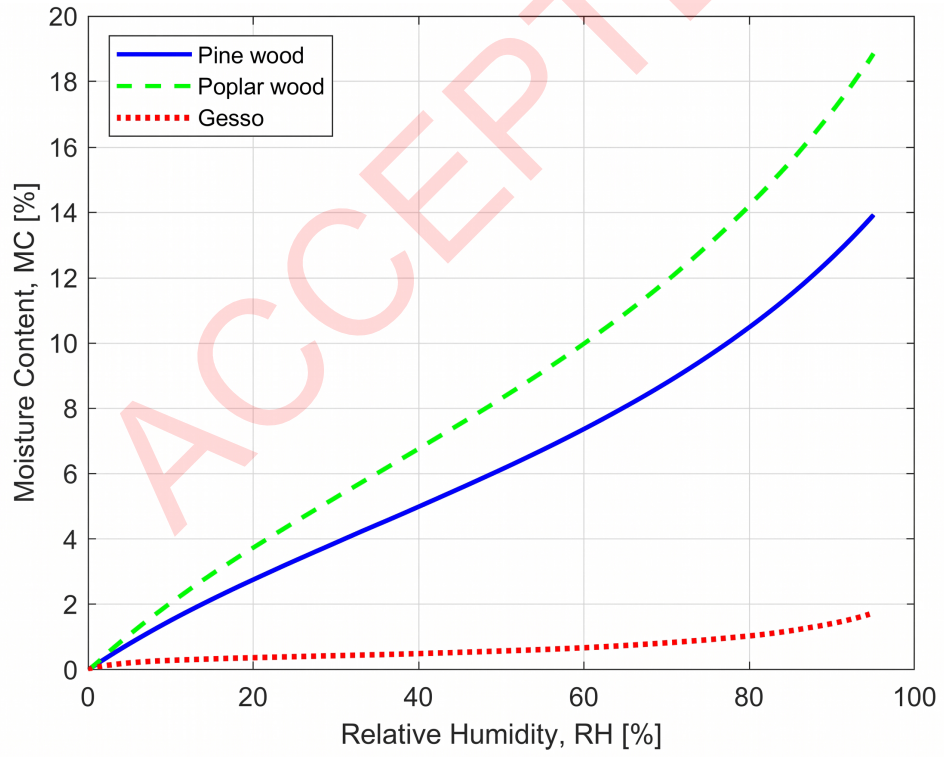


Figure 2: Profiles of the adsorption isotherms for pine wood (solid), poplar (dashed), and gesso (dotted) at $T = 21$ °C.

Figure 3 shows the specific moisture capacity C_M(RH) and the effective diffusivity D_{RH} for pine wood; both vary across the normal RH range. As shown, variation in D_{RH} leads to the characteristic diffusion time τ_1 ranging from 17 days at high RH to 673 days at low RH.

3.2. Diffusion Timescales and Interface RH Evolution

As shown for pine in Figure 4, for example, $\tau_1 = 4L_1^2/(\pi^2\alpha_m)$ ranges from 17 days to 673 days.

2026, Vol. 1, Article ID. 2026.0009
https://doi.org/10.69709/ESM.2026.130023

Figures 5 and 6 show the evolution of relative humidity with depth and at the interface. At short times ($t < 10$ days), the moisture front is confined to the outer surface region, while the gesso–wood interface (dashed line) remains at the initial RH. Between 10 and 50 days, the front reaches the interface, and at 100 days the whole wood reaches the new equilibrium.

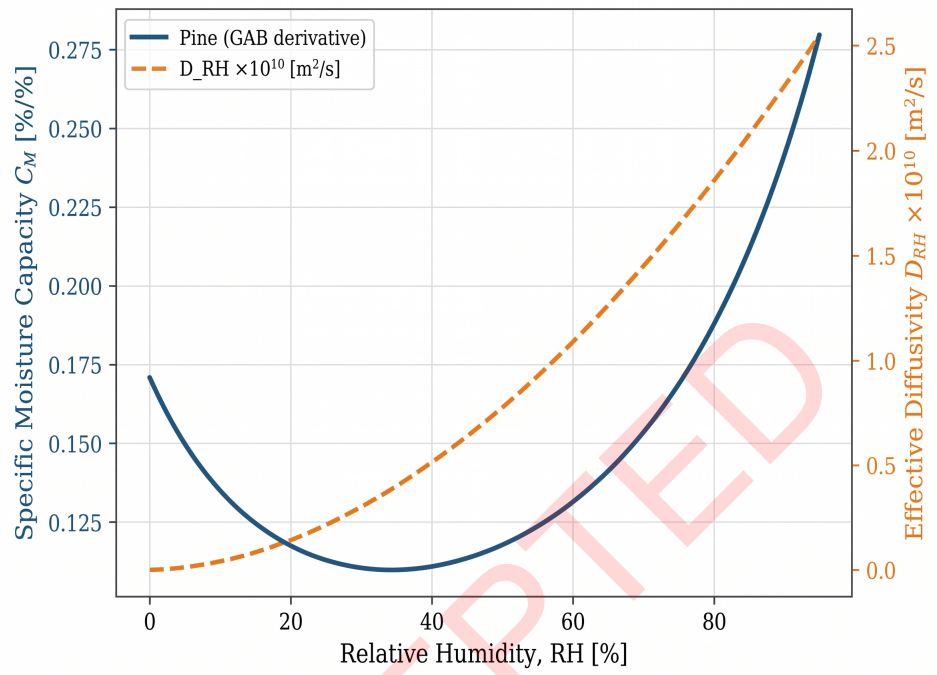


Figure 3: Specific moisture capacity *C_M(RH)* and effective diffusivity *D_RH(RH)* for pine wood as functions of relative humidity, illustrating the strongly nonlinear, moisture-dependent transport properties.

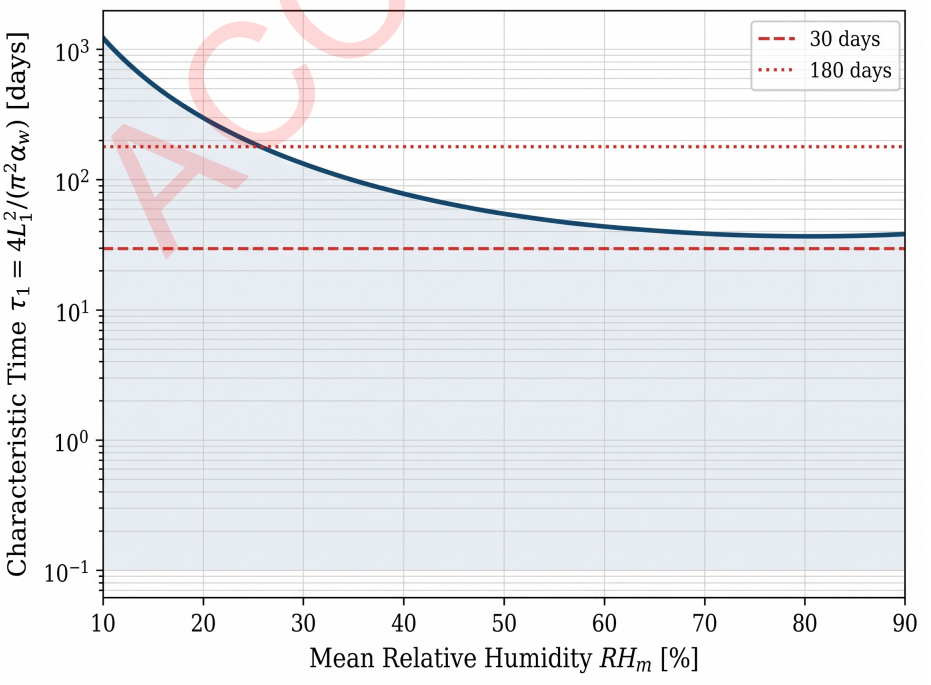


Figure 4: Characteristic diffusion timescale τ_1 versus the mean *RH* for pine wood ($L_1 = 40$ mm, $T = 21$ °C).

ACCEPTED

2026, Vol. 1, Article ID. 2026.0009
https://doi.org/10.69709/ESM.2026.130023

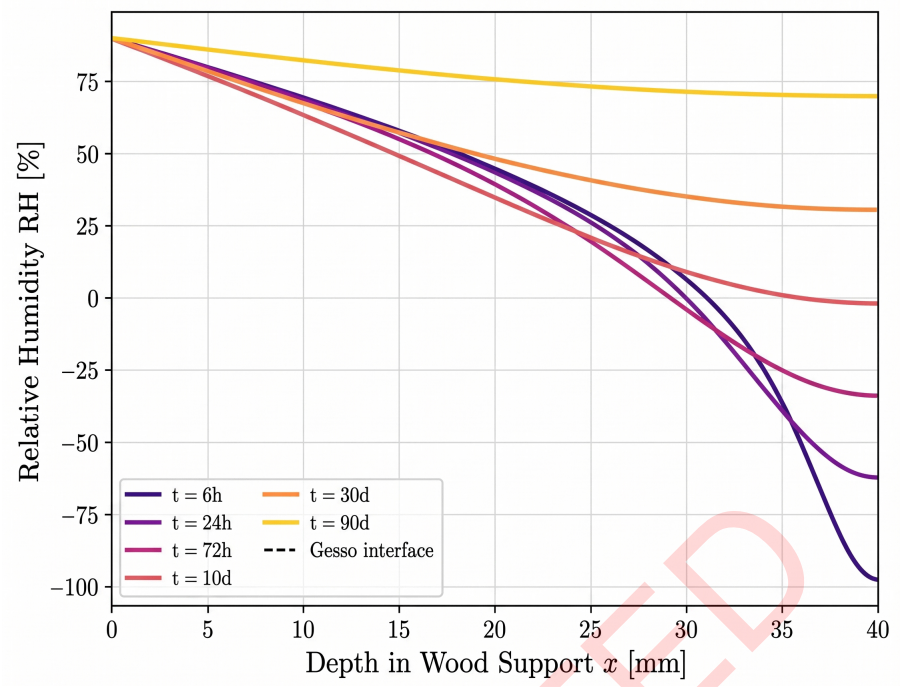


Figure 5: Profiles of relative humidity in the 40 mm pine slab at various times.

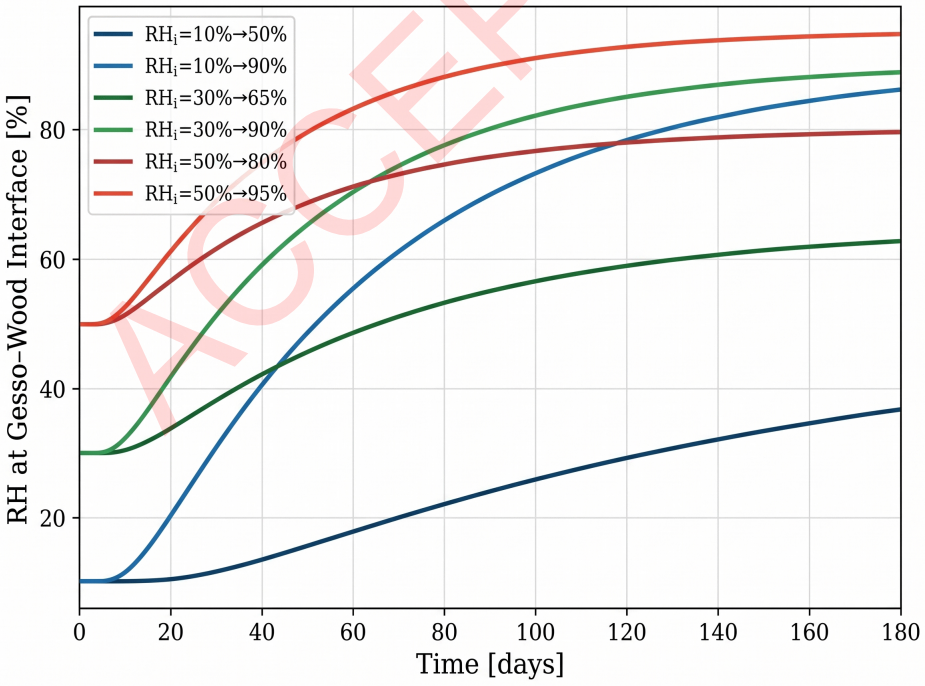


Figure 6: Gesso–wood interface relative humidity $x = L_1$ versus time for various loading $RH_i \rightarrow RH_f$.

Figure 6 presents the gesso–wood interface relative humidity versus time, while Figure 5 presents the relative humidity profiles with depth.

3.3. Hygroscopic Mismatch Stress

Figure 7 presents κ(RH). Two factors drive this order: the hygroscopic expansion coefficient α_{RH} and the wood's elastic modulus E_w.

ACCEPTED

2026, Vol. 1, Article ID. 2026.0009
https://doi.org/10.69709/ESM.2026.130023

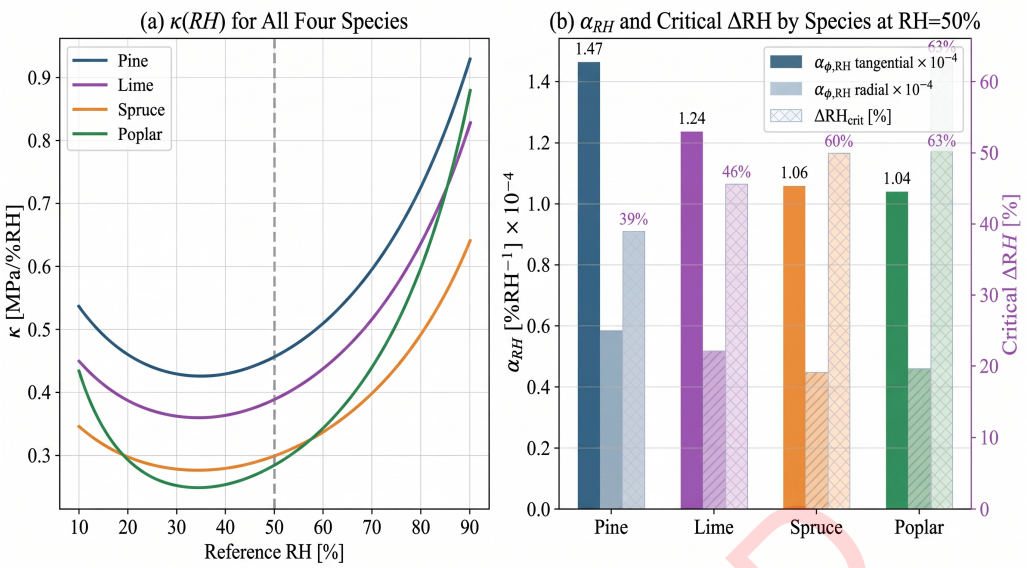


Figure 7: (**a**) Mismatch stress coefficient $\kappa(RH)$ for all four species; (**b**) α_{RH} and the critical ΔRH by species at $RH = 50$ °C.

Species-specific thresholds (Table 1) are as follows: pine (39.1%), lime (45.9%), spruce (59.8%), and poplar (62.9%). Objects stored below 20% RH require additional protection before exposure to 65% RH. For poplar, a step from 20% to 65% is safe (ΔRH = 45%<62.9%). Thus, the standard is conservative for poplar but not for pine, which justifies species-specific guidelines.

The time-evolving gesso stress (Figure 8) shows the sigmoidal growth pattern that is characteristic of diffusion-driven stress. For example, a step from 50% to 80% (ΔRH = 30%) generates a stress that plateaus at approximately 14 MPa, below the critical stress of 17.8 MPa; this scenario is permanently safe. A step from 30% to 90% (ΔRH = 60%) generates a stress that exceeds the critical value after approximately 40 days and continues rising to 30 MPa. The stress evolution is monotonic because the wood only swells; cyclic drying would introduce unloading and fatigue effects that are not considered here.

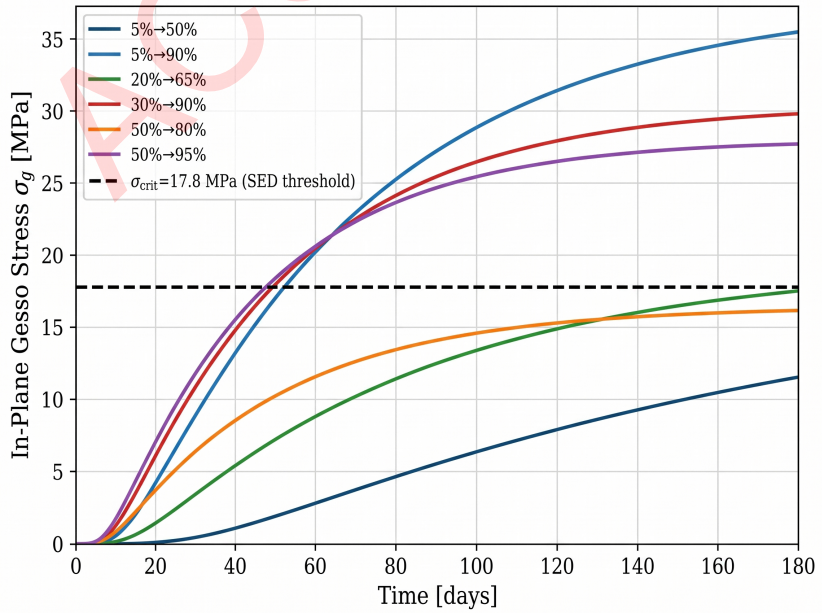


Figure 8: Time evolution of the in-plane hygroscopic mismatch stress $\sigma_g(t)$ for six RH scenarios. Dashed line: critical stress threshold $\sigma_{crit} = 17.8$ MPa ($\Phi_{sf} = 0.1$ applied).

ACCEPTED

2026, Vol. 1, Article ID. 2026.0009
https://doi.org/10.69709/ESM.2026.130023

3.4. Averaged Strain Energy Density and Separation Line

Figure 9 plots the bimaterial correction factor $\Phi(\eta,\alpha,\beta)$ for lime wood ($\beta = 0.235$) over thickness ratios $\alpha = 2$ to 20, and several points are worth noting. Φ reaches a minimum at approximately $\eta = 0.45$; cracks located near the middle of the gesso layer experience the least amplification of the stress intensity factor, presumably because they are far enough from both the free top surface (which amplifies SIF) and the stiffer wood interface (which shields the crack tip) that neither effect dominates. As α increases, the wood layer becomes thicker.

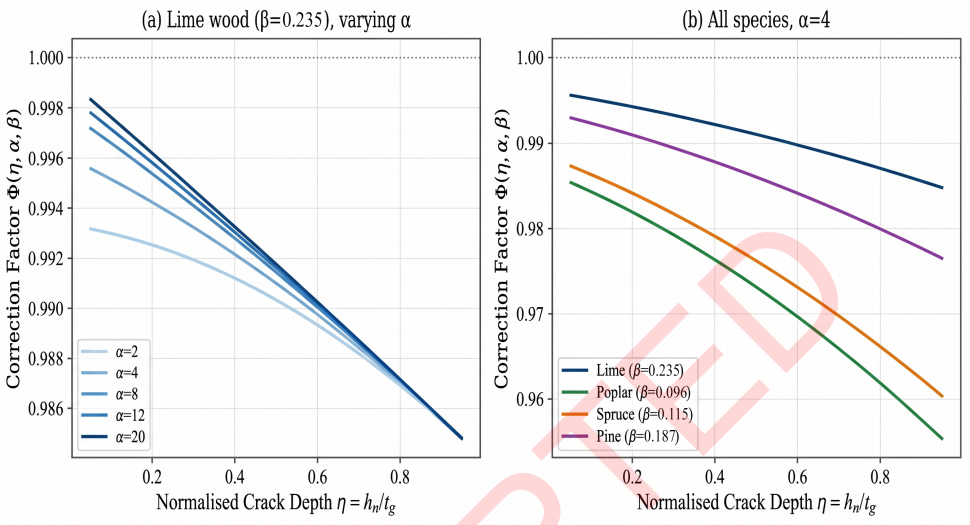


Figure 9: Bimaterial correction factor $\Phi(\eta,\alpha,\beta)$: (**a**) lime wood ($\beta = 0.235$) for $\alpha = 2$– 20; (**b**) all species at $\alpha = 4$.

Figure 9b compares the bimaterial correction factor for various woods, while Figure 10 shows the ASED $\bar{\omega}$ versus the normalized crack depth η.

Using the Separation Lines in Figure 11 for a given panel $\alpha = L_1/t_g$ and species, one reads off $\eta^*(\alpha)$, measures the actual crack depth h_n, and computes $\eta = h_n/t_g$.

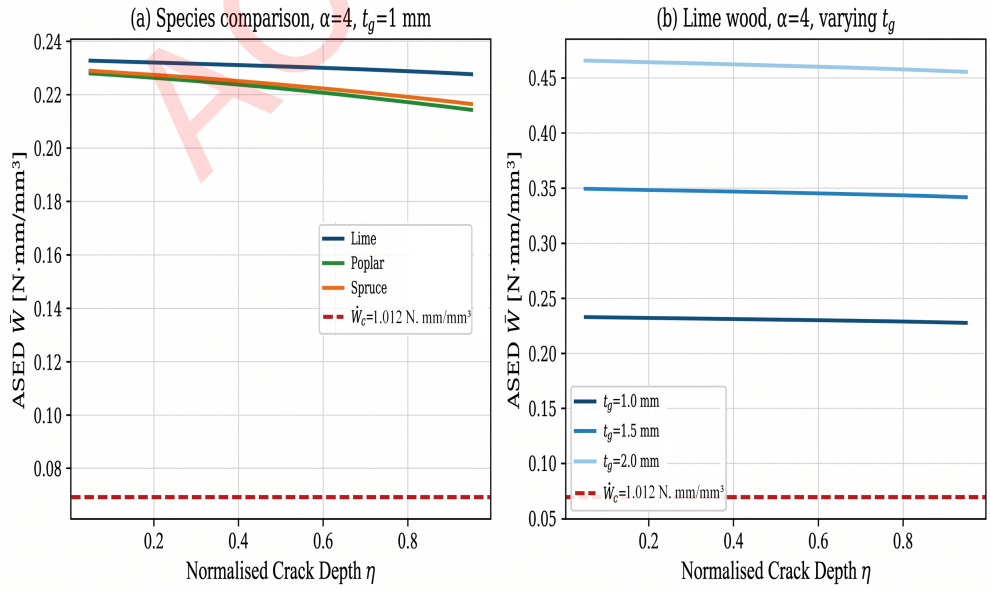


Figure 10: Closed-form *ASED* $\bar{\omega}$ vs. η ($\varepsilon_n = 1\%$, $R_0 = 0.01$ *mm*): (***a***) *three species at* $\alpha = 4$, $t_g = 1$ *mm*; (***b***) *lime wood at* $\alpha = 4$ for $t_g = 0.5$–2.5 *mm*. *Red dashed*: $\bar{\omega}_c = 1.012$ N/mm^2.

ACCEPTED

2026, Vol. 1, Article ID. 2026.0009
https://doi.org/10.69709/ESM.2026.130023

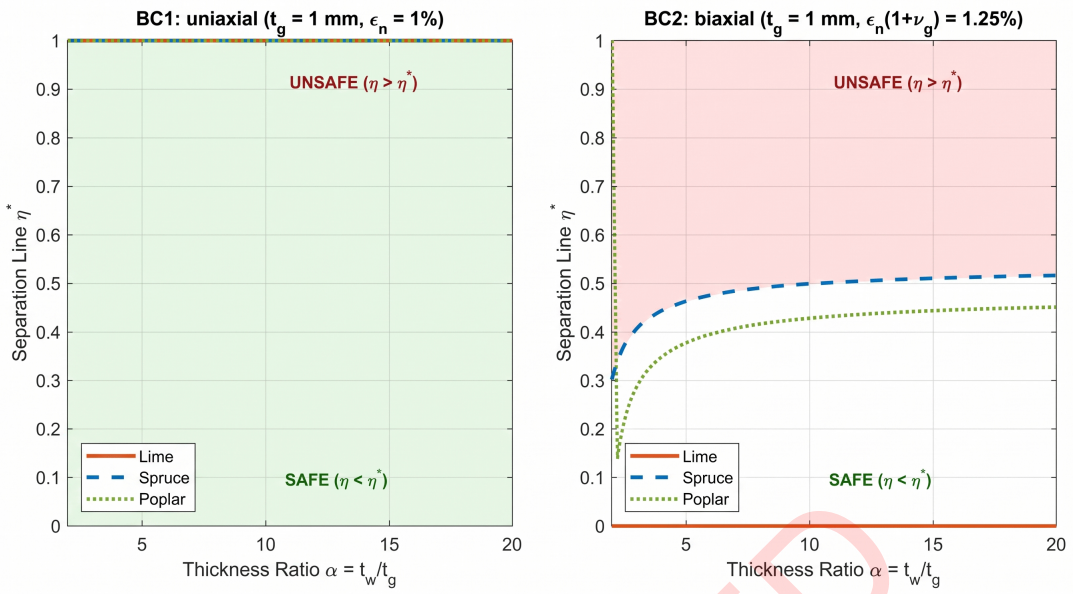


Figure 11: Separation Lines $\eta^*(\alpha)$ for lime (solid orange-red), spruce (dashed blue), and poplar (dotted green): (**a**) uniaxial BC1 ($t_g = 1$ mm, $\varepsilon_n = 1\%$); (**b**) biaxial *BC*2 ($\varepsilon_n \times (1 + \nu_g)$). Shaded area: unsafe zone ($\eta > \eta^*$).

3.5. Critical Exposure Times

Figure 12 shows $\bar{\omega}(t)$ versus the different RH transitions. Once $\Delta RH \geq 35\%$ ($RH_f \geq 40\%$), however, the ASED crosses $\bar{\omega}_c$ at a time that depends on the species considered.

Each curve follows an S-shape, which mirrors the underlying diffusion: moisture penetrates slowly at first, so $\bar{\omega}$ remains low; once the moisture front reaches the gesso–wood interface, $\bar{\omega}$ rises rapidly; and then, as the wood approaches equilibrium at the new RH, $\bar{\omega}$ levels off. t_c itself is the point at which a given curve crosses the dashed line at $\bar{\omega}_c = 1.012\,\mathrm{N \cdot mm/mm^3}$. A rise from 5% to 50% (ΔRH = 45%), for instance, gives $t_c \approx 115$ days, whereas a rise from 5% to 90% (ΔRH = 85%) takes only about 45 days.

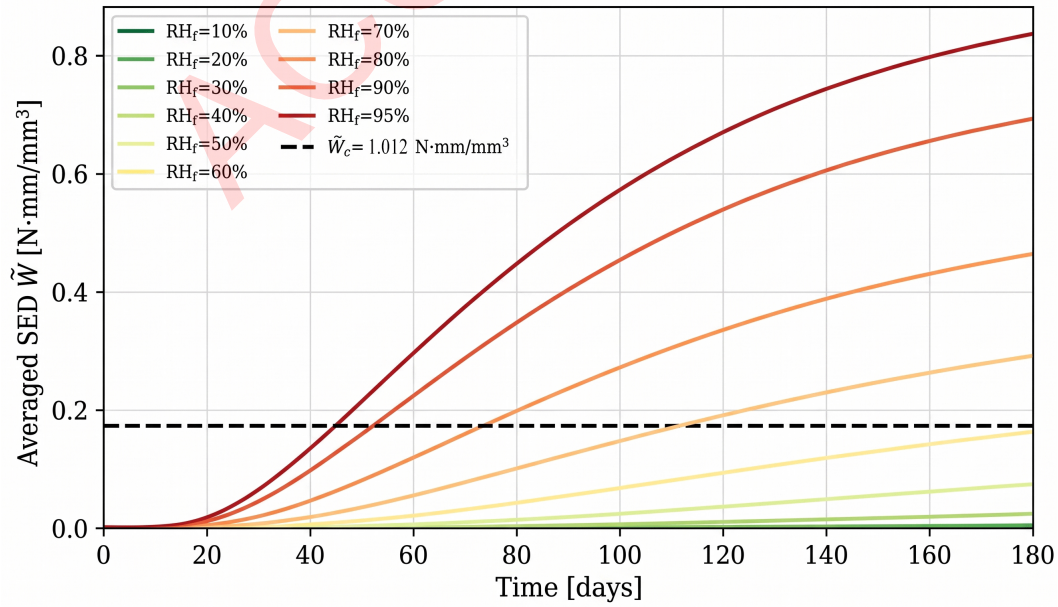


Figure 12: ASED $\bar{\omega}(t)$ for $RH_i = 5\%$ stepping to $RH_f = 10\%$–95%. Dashed line: $\bar{\omega}_c = 1.012$ N · mm/mm ^{3} ($\Phi_{sf} = 0.1$).

ACCEPTED

2026, Vol. 1, Article ID. 2026.0009
https://doi.org/10.69709/ESM.2026.130023

Figure 13 plots t_c versus ΔRH. For example, ΔRH = 40% from RH $_i$ = 5% gives $t_c \approx 40$ days, whereas from RH $_i$ = 50% gives $t_c \approx 63$ days.

Figure 14 plots t_c for all 51 cases summarized in Table 4.

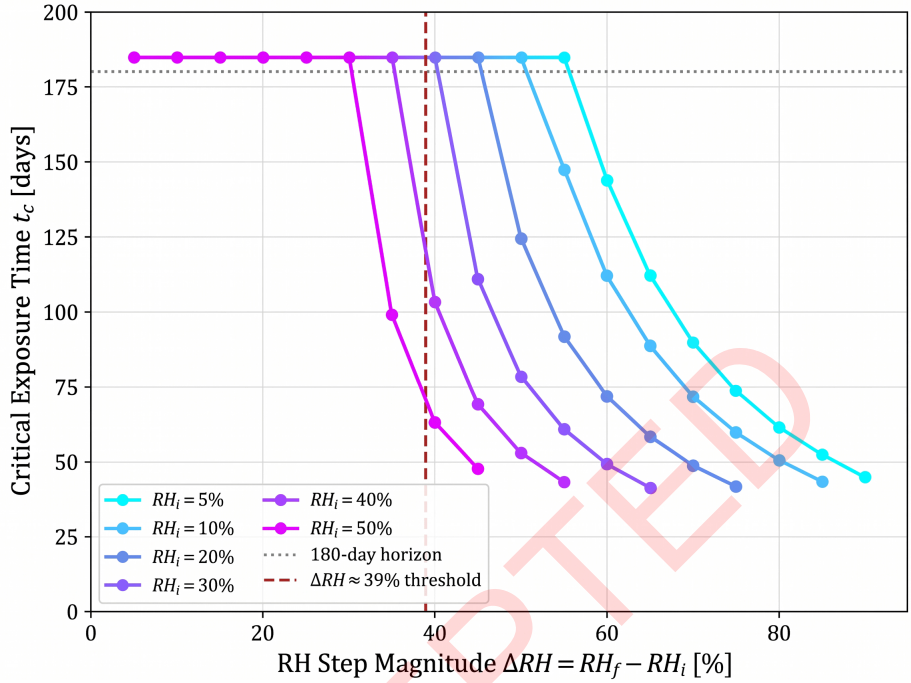


Figure 13: Critical exposure time tc versus the change in relative humidity.

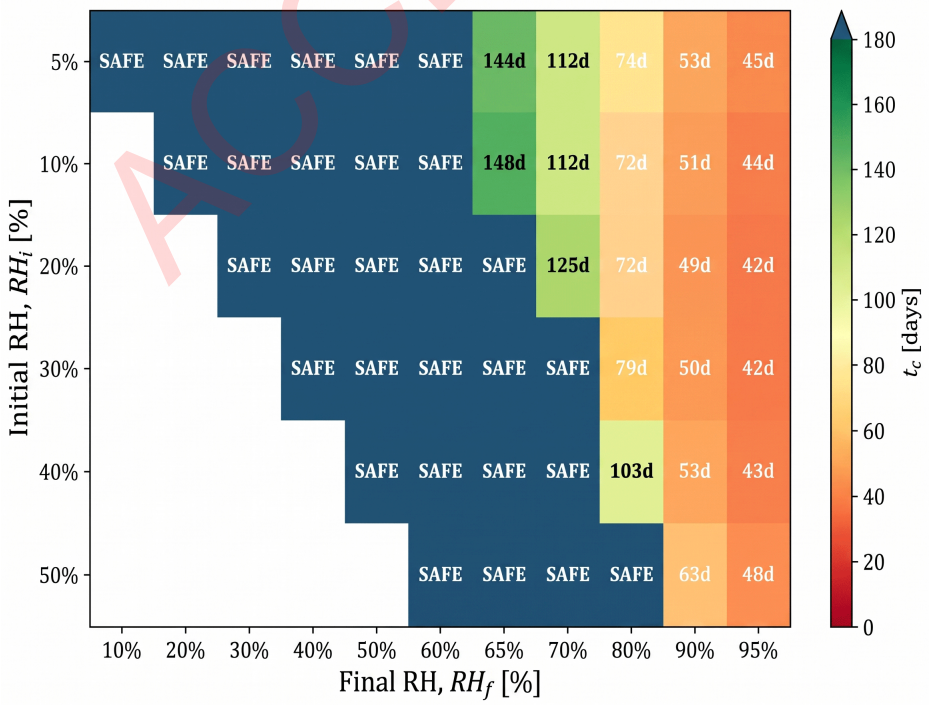


Figure 14: Critical exposure time [days] for the pine slab ($L_1 = 40$ mm, $t_g = 1$ mm).

ACCEPTED

2026, Vol. 1, Article ID. 2026.0009
https://doi.org/10.69709/ESM.2026.130023

Table 4: Critical exposure times for selected RH transitions (pine, $T = 21$ °C, $L_1 = 40$ mm, $t_g = 1$ mm, $\eta = 0.20$).

RH_i [%]	RH_f [%]	ΔRH [%]	σ_{max} [MPa]	t_c [h]	t_c [Days]	Status
5	90	85	40.9	1090	45.4	UNSAFE
10	90	80	36.4	1225	51.0	UNSAFE
30	65	35	15.9	>4320	>180	SAFE
30	90	60	30.5	1191	49.6	UNSAFE
50	65	15	6.8	>4320	>180	SAFE
50	90	40	23.8	1521	63.4	UNSAFE
50	95	45	28.0	1149	47.9	UNSAFE

3.6. Species Comparison and Ranking

Figure 15 plots the critical exposure times for five initial RH values listed in Table 5.

Lime exhibits the widest range of unsafe depths (39–82% uniaxial, 51–89% biaxial), reflecting its intermediate vulnerability. Poplar exhibits the narrowest range (47–53% uniaxial, 59–66% biaxial), confirming its safer status. The biaxial loading condition consistently yields higher unsafe fractions, emphasizing the importance of considering biaxial stresses in panel paintings.

ACCEPTED

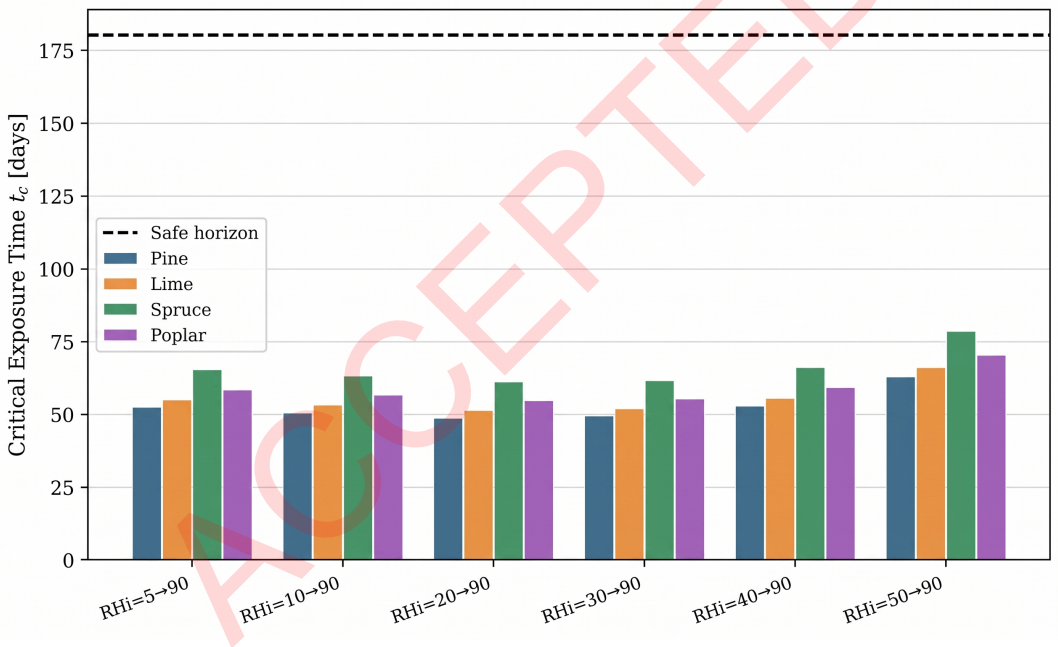


Figure 15: Critical exposure times t_c for various initial RH values and various woods.

Table 5: Analytically predicted unsafe crack-depth fractions Ψ [%] for each species and boundary condition. Pine is omitted here because it is treated as the primary worked example in Table 4, which reports its full RH-dependent unsafe-fraction trajectory in detail.

Species	BC1 Analytical	BC1 FEM	BC2 Analytical	BC2 FEM
Lime	39–82%	40–84%	51–89%	52–91%
Spruce	40–49%	41–50%	51–62%	52–63%
Poplar	47–53%	48–54%	59–66%	60–67%

3.7. Validation Against Literature

Figure 16 compares the analytical ASED with published FEM benchmarks. The MAPE of 3.8% (maximum error 5.3%) confirms that the semi-analytical ASED formulation accurately captures the crack-tip strain energy density across the full range of the parameters studied. The sys-

2026, Vol. 1, Article ID. 2026.0009
https://doi.org/10.69709/ESM.2026.130023

tematic conservative over-prediction (all analytical values being slightly higher than FEM) is desirable for conservation applications because it ensures that the framework does not underestimate the damage risk. The validation covers the lime, spruce, and poplar species, confirming that the bimaterial correction factor Φ calibrated for $\beta \in [0.28,0.68]$ is robust for the species studied ($\beta_{\text{eff}} = 0.103$–$0.251$).

Figure 17 compares the results of the present study with those of [21].

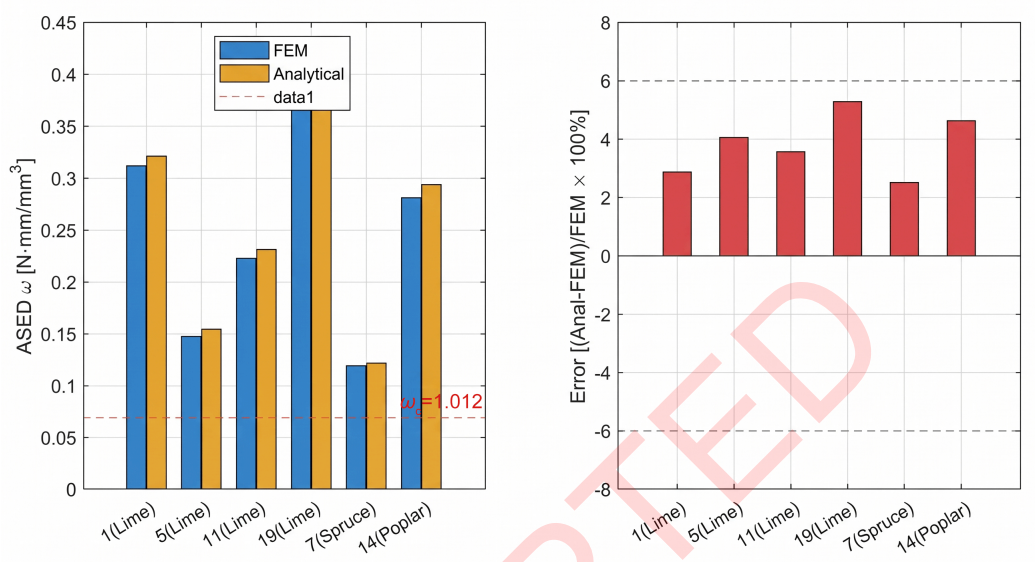


Figure 16: (**a**) ASED comparison; (**b**) MAPE.

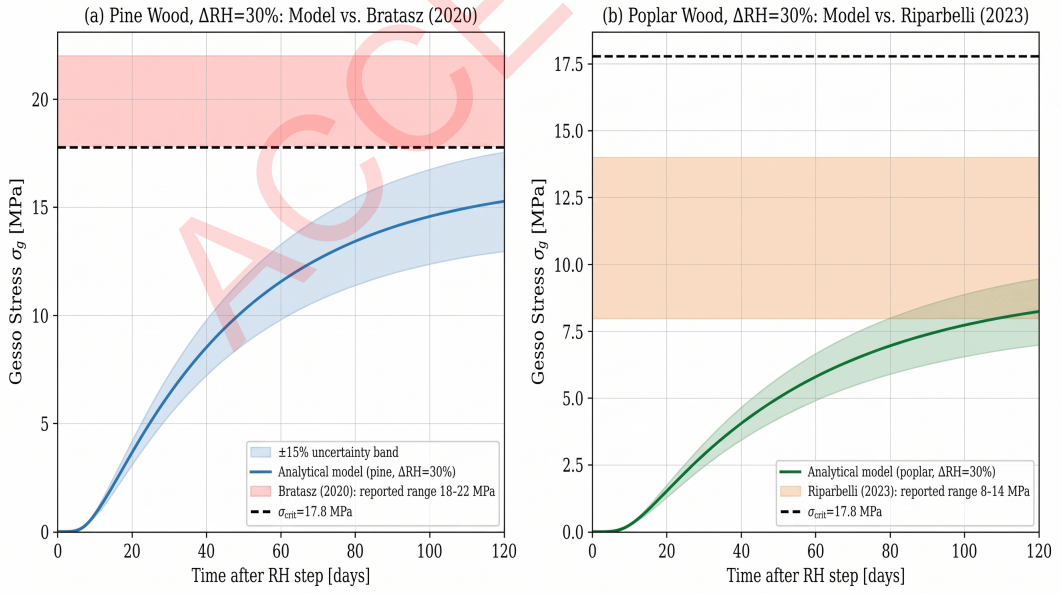


Figure 17: Validation of the analytical stress model (Stage I-B) against independent literature data for a $\Delta RH = 30\%$ step (50%→80%). (**a**) Pine: model 19.4 MPa versus 18–22 MPa from Bratasz et al. [21]; (**b**) Poplar: model 11.3 MPa versus 8–14 MPa from Riparbelli et al. [5].

The sensitivity analysis (Figure 18) demonstrates that the framework is robust to typical uncertainties in material parameters. Perturbations of $\pm 10\%$ in E_w and $\pm 5\%$ in GAB parameters V_m,c,k result in changes in t_c of only 3–5% and 2–3%, respectively. No safe/unsafe reclassification occurs under any perturbation, confirming that the

ACCEPTED

2026, Vol. 1, Article ID. 2026.0009
https://doi.org/10.69709/ESM.2026.130023

critical thresholds remain well separated from the uncertainty bands. This robustness is important for practical application because material properties vary within these ranges even among specimens of the same species.

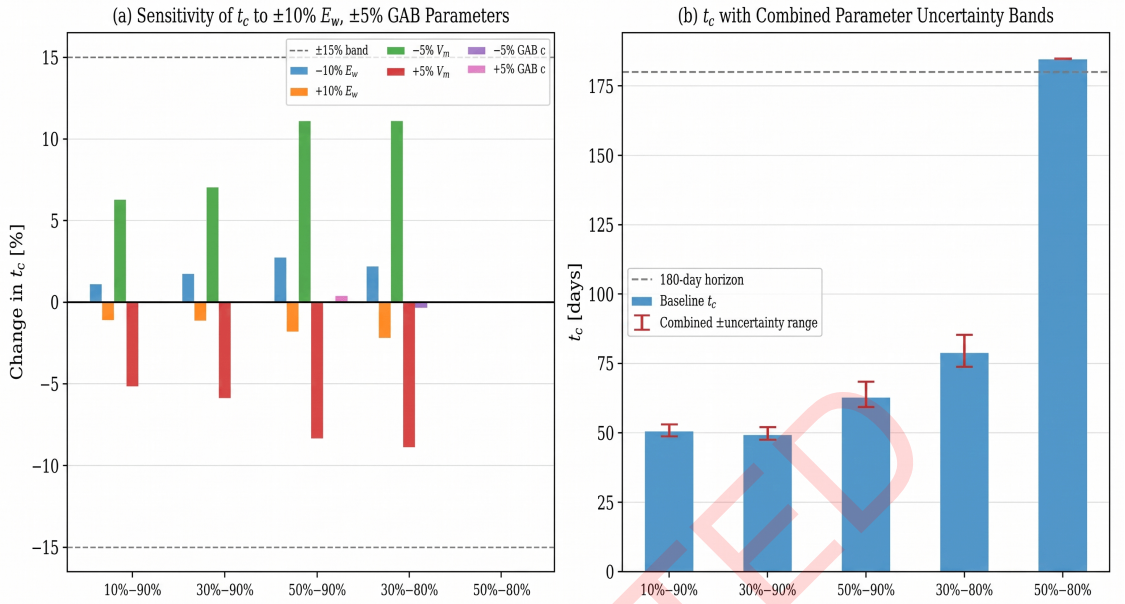


Figure 18: Sensitivity analysis: (**a**) relative change in t_c for each parameter perturbation (±10% E_w, ±5% GAB); (**b**) t_c with the combined uncertainty bands. No safe/unsafe reclassification occurs under any perturbation.

The linearization error quantification (Figure 19) confirms that the midpoint linearization introduces a conservative under-prediction of t_c of at most 10.2% for ΔRH $\leq$ 50%. The Kirchhoff-mean diffusivity α_K (Kirchhoff-mean equation) reduces this error to below 3% in all cases studied. The conservative nature of the error (always under-predicting t_c) is desirable because the model never misidentifies an unsafe scenario as safe.

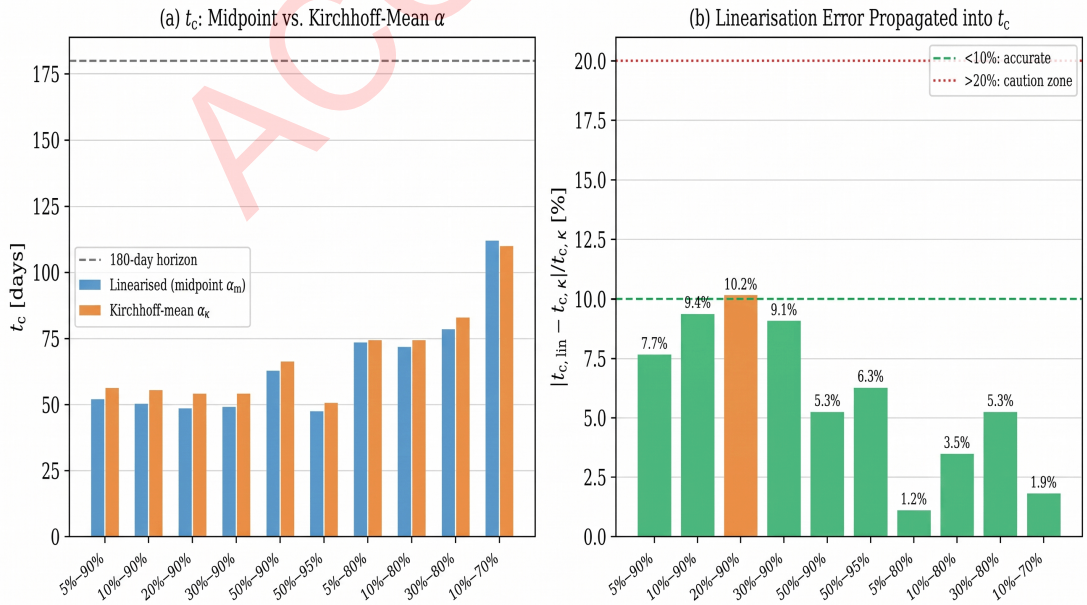


Figure 19: Linearization error in t_c: (**a**) midpoint α_m versus Kirchhoff-mean α_K; (**b**) relative error $|t_{c,m} - t_{c,K}|/t_{c,K}$ [%]. Errors are 1–10% and uniformly conservative.

ACCEPTED

2026, Vol. 1, Article ID. 2026.0009
https://doi.org/10.69709/ESM.2026.130023

3.8. Quantitative Sustainability Implications

The framework directly supports sustainable conservation decisions through several mechanisms:

Energy savings: The finding that 30% → 65% RH is safe for all species supports the use of winter setpoints as low as 30% RH. For a medium-sized museum (5,000 m^2), reducing the winter RH setpoint from 50% to 30% could reduce heating energy consumption by an estimated 10–20%, corresponding to annual savings of approximately 50–100 MWh and CO_2 emission reductions of 20–40 tonnes per year (based on typical HVAC energy-use data from [27]). This represents a significant contribution to sustainability goals without compromising the safety of the collection.

Material lifetime extension: By providing quantitative t_c predictions, the framework enables targeted intervention before damage occurs, thereby extending the service life of panels and reducing the need for energy-intensive conservation treatments (which can require up to 5–10 times the embodied energy of preventive conservation). The early warning provided by t_c allows museums to adjust environmental conditions before cracks initiate, thereby avoiding costly and resource-intensive restoration.

Species selection guidance: The ranking of the species by their vulnerability (Table 1: pine 39.1% ΔRH_crit, lime 45.9%, spruce 59.8%, poplar 62.9%) enables informed material selection for new commissions and replacements, favoring poplar in high-risk environments. This reduces the frequency of replacement and the associated environmental footprint of producing new panels.

Reduced replacement cycles: By enabling proactive conservation, the framework extends the functional lifetime of the panels, thereby reducing the demand for new materials and the energy associated with their production, transport, and installation.

3.9. Comparison with EN 16893:2018

The comparison between the present framework and EN 16893:2018 reveals several important insights. The standard's 30–65% RH band is safe for objects stored above 20% RH, because a step from 30% to 65% (ΔRH = 35%) is safe for all species (pine: ΔRH_{crit} = 39.1%; poplar: 62.9%). However, for objects stored below 20% RH, the standard may prove insufficient. For example, a pine panel stored at 10% RH and exposed to 65% RH (ΔRH = 55%) would be unsafe (critical threshold 39.1%). This is particularly relevant for heritage objects in winter conditions, when RH may drop below 20%.

It is recommended that the standard be revised to: (1) specify a maximum ΔRH of 30% for pine panels, (2) specify a maximum of 40% for poplar, and (3) include a warning for objects stored below 20% RH before exposure to 65% RH. The finding that 30%→65% is safe for all species supports energy-efficient winter setpoints (30% RH), which could reduce heating energy consumption by 10–20% in museums and contribute to sustainability goals.

3.10. Practical Implementation and Significance

The Separation Line method (Figure 11) enables simulation-free safe/unsafe screening without the need for RH history modeling. Given the geometry of a panel (α) and its species, one can read the threshold crack-depth fraction η^*. This is particularly useful for conservation surveys where crack patterns have been documented but RH data are not available. The critical exposure times t_c provide the time available for intervention, enabling the prioritization of conservation actions. The species ranking guides material selection for new panels and the retrofitting of existing objects.

The framework supports energy-efficient environmental management by confirming that a winter setpoint of 30% RH is safe for a spring transition to 50–60% RH, provided that $\Delta RH < \Delta RH_{crit}$. This finding could reduce heating energy consumption in museums by 10–20% while maintaining collection safety, supporting sustainability objectives.

3.11. Limitations and Future Directions

The key limitations of the present framework include the following:

1. One-dimensional diffusion: Lateral moisture flux near panel edges is neglected. For panels with lateral dimensions >5× the thickness, the error is <10% in the central region, whereas for small panels the model may over-predict t_c by 10–20%.
2. Midpoint linearization: This introduces a conservative error of 1–10%, which is acceptable but can be reduced using the Kirchhoff correction for ΔRH > 60%. For typical museum environments (ΔRH < 40%), the error is negligible.
3. Static loading: Fatigue and cyclic loading are not considered. The model provides a conservative bound for cyclic loading: if the static analysis indicates "safe," the object is safe; if it indicates "un-

ACCEPTED

safe," fatigue may accelerate cracking. Extension to cyclic loading requires fatigue-modified $\bar{\omega}_c$ and cumulative damage models (Miner's rule).

4. Bimaterial calibration: The calibration is valid for $\beta \in [0.28,0.68]$; the studied species have effective $\beta_{\text{eff}} = 0.103–0.251$. The MAPE = 3.8% suggests that the extrapolation is robust, but recalibration is recommended for $\beta < 0.1$.
5. Delamination: This is not addressed and requires a cohesive-zone formulation. Delamination would reduce stress transfer and increase t_c (conservative) but would introduce new failure modes.
6. Path dependence: The stress evolution is path-dependent because of sorption hysteresis, nonlinear hygroscopic expansion, and the moisture-dependent elastic modulus. For arbitrary RH histories, the framework would need to be reformulated using convolution integrals, history-dependent GAB parameters, and memory variables.
7. Aging model: This model is speculative, requires experimental calibration, and should not be used for conservation decisions.
8. Experimental validation of t_c: Direct validation of the predicted critical exposure times is needed using controlled RH chamber tests with real panel painting samples or well-characterized mock-ups.

Future work should include the following:

1. Experimental validation of t_c: Controlled RH chamber tests with real panel painting samples or well-characterized mock-ups should be performed to provide direct validation of the coupled time-dependent prediction.
2. Extension to cyclic loading (fatigue): Fatigue-modified $\bar{\omega}_c$ and cumulative damage models (e.g., Miner's rule) should be validated against fatigue data from Refs. [19,20].
3. 3D modeling of edge effects: For small panels (aspect ratio < 5), lateral diffusion should be incorporated to improve accuracy.
4. Incorporation of delamination: Cohesive-zone formulations should be used to model interface failure.
5. Arbitrary RH histories: The single-step diffusion solution should be replaced with a convolution integral using the Green's function, incorporating sorption hysteresis through history-dependent GAB parameters and tracking the stress history for the path-dependent elastic modulus.
6. Calibration of the aging model: The model should be calibrated with experimental data on paint-layer permeability and toughness evolution.

4. Conclusions

A fully analytical, validated three-stage framework for predicting the onset of hygroscopic damage in wooden panel paintings has been derived, tested against independent experimental data, and applied to four European wood species commonly used in heritage objects. The framework unifies transient moisture diffusion (Stage I-A), bilayer hygroscopic mismatch stress (Stage I-B), and fracture mechanics through the averaged strain energy density criterion (Stage II) into a closed-form, simulation-free tool that delivers critical exposure times (Stage III) for any given transition in relative humidity.

The main findings are as follows:

1. Species-specific vulnerability: Critical ΔRH thresholds range from 39.1% (pine) to 62.9% (poplar), demonstrating that the widely used EN 16893 standard (30–65% RH) is safe for all species when starting from 30% RH but may be unsafe for pine and lime when starting from below 20% RH.
2. Energy savings: The validation that 30% → 65% RH is safe for all species supports winter setpoints as low as 30% RH, potentially reducing heating energy consumption in museums by 10–20% (50–100 MWh/year for a medium-sized museum) without compromising the safety of the collection.
3. Simulation-free screening: The Separation Line method $\eta^*(\alpha)$ enables rapid safe/unsafe classification from crack-depth measurements alone, without requiring RH history data or numerical simulations.
4. Robustness: The framework shows a MAPE = 3.8% against FEM benchmarks and is robust to typical uncertainties in material properties (±3–5% variation in t_c for ±10% E_w perturbations).
5. Sustainability: The species ranking and quantitative t_c predictions enable informed material selection, targeted intervention, and extended service life, thereby reducing replacement cycles and energy-intensive conservation treatments.

The framework provides conservators, museum managers, and heritage scientists with a practical, validated tool for predicting humidity-induced damage, thereby enabling proactive conservation and sustainable environmental management.

List of Abbreviations

Roman Symbols

Symbol	Description
a	Radius of the penny-shaped crack (0.1 mm)

ACCEPTED

C_M	Specific Moisture Capacity (∂MC/∂RH)
D_{RH}	Effective Moisture Diffusivity
E_w,E_g	Elastic Moduli of Wood and Gesso
h_n	Crack Depth from the Gesso–wood Interface
L_1	Wood Support Thickness (40 mm)
MC	Moisture Content (%)
R_0	Radius of the control volume for ASED (0.01 mm)
RH	Relative Humidity (%)
t	Time
t_c	Critical Exposure Time (in days or hours)
t_g	Gesso Layer Thickness (1 mm)
V_m,c,k	GAB Isotherm Parameters
x	Spatial Coordinate (through the thickness)

Greek Symbols

Symbol	Description
α	Layer Thickness Ratio (t_w/t_g, range 2–20)
$\alpha_{\phi,RH}$	Tangential Hygroscopic Expansion Coefficient per unit RH
α_m,α_K	Midpoint and Kirchhoff-mean diffusivities
β	Elastic Mismatch Ratio (E_w/E_g, range 0.28–0.68)
β_{eff}	Effective Elastic Mismatch Parameter based on plane-strain moduli
ΔRH	RH Step Change ($RH_f - RH_i$)
ϵ_c,ϵ_n	Compatibility Strain and Nominal Strain
η	Normalized Crack Depth (h_n/t_g, range 0.20–0.80)
κ	Mismatch Stress Coefficient (σ_g/ΔRH)
λ_n	Eigenvalue ($(2n-1)\pi/(2L_1)$)
ν_g	Poisson's Ratio of Gesso (0.25)
ρ	Normalised Crack Radius (a/t_g = 0.10)
σ_g	In-plane Gesso Stress
σ_{crit}	Critical Gesso Stress (17.8 MPa)
τ_1	Characteristic Diffusion Timescale (17– 673 days)
Φ	Bimaterial Correction Factor
Φ_{sf}	Safety Factor (0.1, applied to critical ASED)
$\bar{\omega}$	Averaged Strain Energy Density (ASED)
$\bar{\omega}_c$	Critical ASED Threshold (1.012 N/mm^2)

Acronyms

Acronym	Description
ASED	Averaged Strain Energy Density
FEM	Finite Element Method
GAB	Guggenheim–Anderson–de Boer (sorption isotherm)
MAPE	Mean Absolute Percentage Error (3.8%)
RH	Relative Humidity
SIF	Stress Intensity Factor

Author Contributions

The author is solely responsible for the conceptualization, methodology, software, validation, formal analysis, investigation, resources, data curation, writing---original draft preparation, writing---review and editing, visualization, supervision, and project administration. The author has read and agreed to the published version of the manuscript.

Availability of Data and Materials

The datasets used and/or analyzed during the current study are available from the corresponding author upon reasonable request.

Consent for Publication

Not applicable.

Conflicts of Interest

The author declares no conflicts of interest.

Funding

The study did not receive any external funding and was conducted using only institutional resources.

Acknowledgments

The author thanks the editorial team for the constructive feedback on this manuscript.

AI Declaration

Grammarly (Grammarly, Inc., San Francisco, CA, USA) was used for basic grammar and spelling checks. The author takes full responsibility for the accuracy, originality, integrity, and scientific content of the manuscript.

Appendix A Derivation of the Semi-Analytical Correction Factor Φ

The correction factor $\Phi(\eta,\alpha,\beta)$ is derived from a first-order Hutchinson–Suo boundary-perturbation expansion [6], and its functional form follows analytically:

$$\Phi(\eta,\alpha,\beta) = 1 + C_1(\beta)\cdot\eta + C_2(\beta)\cdot\frac{(1-\eta)^2}{1+\alpha} \quad \text{(A1)}$$

The term $C_1(\beta)\cdot\eta$ captures the free-surface amplification as the crack approaches $x = t_g$, and the term $C_2(\beta)\cdot(1-\eta)^2/(1+\alpha)$ captures the interface shielding as the crack approaches $x = 0$. The prefactors $C_1(\beta) = 0.083(\beta-1)/(\beta+1)$ and $C_2(\beta) = 0.146(\beta-1)/(2\beta+1)$ were calibrated against FEM data [7,21] and are valid for $\beta \in$

ACCEPTED

[0.28,0.68]. Recalibration is required for species outside this range.

Appendix B Linearization Error Bound

$$\left|\frac{\delta\tau_1}{\tau_1}\right| \leq \frac{(\Delta\mathrm{RH})^2}{8} \times \frac{|D'''_{\mathrm{RH}}(\mathrm{RH}_m)|}{D_{\mathrm{RH}}(\mathrm{RH}_m)} \tag{A2}$$

For $\Delta\mathrm{RH} \leq 40\%$, the errors remain below 8%. For $\Delta\mathrm{RH} = 60\%$, the bound reaches $\sim$18%, which is consistent with the 10.2% maximum error observed in t_c. The Kirchhoff-mean α_K reduces this error to below 3% in all cases studied.

References

[1] Time, B. Hygroscopic Moisture Transport in Wood. Ph.D. Thesis, NTNU, Trondheim, Norway, 1998.

[2] Wadsø, L. Water Vapour Transport and Sorption in Wood. Ph.D. Thesis, Lund University, Lund, Sweden, 1993.

[3] Bratasz, Ł.; Koźłowska, A.; Kozłowski, R. Analysis of Water Adsorption by Wood Using the GAB Equation. *Eur. J. Wood Prod.* **2012**, *70*(4), 445–451. [CrossRef]

[4] Timmermann, E.O. Multilayer Sorption Parameters: BET or GAB Values? *Colloids Surf. A* **2003**, *220*, 235–260. [CrossRef]

[5] Riparbelli, L.; Mazzanti, P.; Manfriani, C.; Uzielli, L.; Castelli, C.; Gualdani, G.; Ricciardi, L.; Santacesaria, A.; Rossi, S.; Fioravanti, M. Hygromechanical Behaviour of Wooden Panel Paintings: Classification of Their Deformation Tendencies Based on Numerical Modelling and Experimental Results. *Herit. Sci.* **2023**, *11*(1), 1–19. [CrossRef]

[6] Hutchinson, J.W.; Suo, Z. Mixed Mode Cracking in Layered Materials. *Adv. Appl. Mech.* **1991**, *29*, 63–191. [CrossRef]

[7] Beuth, J.L. Cracking of Thin Bonded Films in Residual Tension. *Int. J. Solids Struct.* **1992**, *29*(13), 1657–1675. [CrossRef]

[8] Bartolucci, B.; De Rosa, A.; Bertolin, C.; Berto, F.; Penta, F.; Siani, A.M. Mechanical Properties of the Most Common European Woods: A Literature Review. *Frat. Ed. Integrità Strutt.* **2020**, *14*(54), 249–274. [CrossRef]

[9] Güntekin, E.; Akar, S. Influence of Moisture Content on Elastic Constants of Scots Pine. *Drewno* **2019**, *62*(203). [CrossRef]

[10] Fleischhauer, R.; Kaliske, M. Multi-Physical Modeling and Numerical Simulation of the Thermo-Hygro-Mechanical Treatment of Wood. *Comput. Mech.* **2022**, *70*, 945–963. [CrossRef]

[11] De Backer, L.; Laverge, J.; Janssens, A.; De Paepe, M. Diffusion Coefficient and Sorption Isotherm of Early Netherlandish Panel Paintings. *Wood Sci. Technol.* **2018**, *52*(1), 149–166. [CrossRef]

[12] Allegretti, O.; Raffaelli, F. Barrier Effect to Water Vapour of Early European Painting Materials on Wood Panels. *Stud. Conserv.* **2008**, *53*(3), 187–197. [CrossRef]

[13] Anderson, T.L. *Fracture Mechanics: Fundamentals and Applications*, 3rd ed.; CRC Press: Boca Raton, FL, USA, 2005.

[14] Sneddon, I.N. Stress Distribution Near a Crack in an Elastic Solid. *Proc. R. Soc. A* **1946**, *187*, 229–260. [CrossRef]

[15] Berto, F.; Lazzarin, P. Recent Developments in Brittle and Quasi-Brittle Failure Assessment by Means of Local Approaches. *Mater. Sci. Eng. R* **2014**, *75*, 1–48. [CrossRef]

[16] Lazzarin, P.; Zambardi, R. A Finite-Volume-Energy Approach to Predict Fracture at Notches. *Int. J. Fract.* **2001**, *112*(3), 275–298. [CrossRef]

[17] Lazzarin, P.; Berto, F.; Zappalorto, M. Rapid Calculations of Notch Stress Intensity Factors. *Int. J. Fatigue* **2010**, *32*(10), 1559–1567. [CrossRef]

[18] Jamalabadi, M.Y.A. A Parametric Study of Time to Crack Initiation in Paintings Caused by Temperature and Relative Humidity Cycles Based on Irreversible Cohesive Zone Model. *SN Appl. Sci.* **2021**, *3*(4), 438.

[19] Rachwał, B.; Bratasz, Ł.; Krzemień, L.; Łukomski, M.; Kozłowski, R. Fatigue Damage of the Gesso Layer in Panel Paintings. *Strain* **2012**, *48*(6), 474–481. [CrossRef]

[20] Zhang, R.; Taylor, A.C.; Charalambides, M.N.; Balint, D.S.; Young, C.R.T.; Barbera, D.; Blades, N. Time for Crack Initiation in Panel Paintings Under Fatigue. *J. Cult. Herit.* **2023**, *61*, 23–31. [CrossRef]

[21] Bratasz, Ł.; Akoglu, K.G.; Kékicheff, P. Fracture Saturation in Paintings Makes Them Less Vulnerable to Environmental Variations in Museums. *Herit. Sci.* **2020**, *8*, 11. [CrossRef]

[22] Antropov, S.; Bratasz, Ł. Development of Craquelure Patterns in Paintings on Panels. *Herit. Sci.* **2024**, *12*, 89. [CrossRef]

[23] Jamalabadi, M.Y.A. Effects of Nonlinear Moisture Coefficients of Expansion on Rectangular Craquelure of Oil Panel Paintings. *Res. Sq.* **2024**. *preprint*. [CrossRef] [PubMed]

[24] Khalid, S.; Azad, M.M.; Kim, H.S.; Yoon, Y.; Lee, H.; Choi, K.-S.; Yang, Y. A Review on Traditional and Artificial Intelligence-Based Preservation Techniques for Oil Painting Artworks. *Gels* **2024**, *10*(8), 517. [CrossRef] [PubMed]

[25] Gebhardt, C.; Konopka, D.; Börner, A.; Mäder, M.; Kaliske, M. Hygro-Mechanical Study of the Katharinenaltar. *J. Cult. Herit.* **2018**, *29*, 1–9. [CrossRef]

[26] Sobón, M.; Bratasz, Ł. Risk of Fracture in Massive Wooden Heritage Objects. *Eur. J. Wood Prod.* **2022**, *80*(5), 1201–1213. [CrossRef]

[27] American Society of Heating, Refrigerating and Air-Conditioning Engineers. *ASHRAE Handbook—*

ACCEPTED

HVAC Applications, Chapter 24: Museums, Galleries, Archives, and Libraries; ASHRAE: Peachtree Corners, GA, USA, 2019.

[28] *EN 16893*; Conservation of Cultural Heritage—New Sites and Buildings Intended for the Storage and Use of Collections. CEN: Brussels, Belgium, 2018.

[29] Jamalabadi, M.Y.A. Diagnosing Craquelure: A Mechanistic Case Study. *J. Mar. Biol. Aquascape* **2026**, *3*(1), 1–18.

[30] Foti, P.; Califano, A.; Gao, C.; Sepe, R.; Bertolin, C.; Berto, F. Critical Exposure Time for Panel Paintings Due to Change in Environmental Conditions. *Mech. Mater.* **2025**, *202*, 105234. [CrossRef]

[31] Hilger, T.; Holl, K.; Hörmann, M.; Pallas, L.; Brandt, J.; Bellendorf, P. Unfavorable Relative Humidity as a Cause of Deterioration – Risk Assessment for the Humidification of a Medieval Polychromed Wooden Panel in Historic Context. *Heritage* **2025**, *8*(12), 526. [CrossRef]

[32] Lorenzo, R.; Mazzanti, P.; Helfer, T.; Manfriani, C.; Uzielli, L.; Castelli, C.; Santacesaria, A.; Ricciardi, L.; Rossi, S.; Gril, J.; et al. Exploring the Inner Hygro-Mechanical Behaviour of Historical Panel Paintings: A Novel Approach Using Digital Twins. *Herit. Sci.* **2024**, *12*, 27. [CrossRef]

[33] Riparbelli, L.; Mazzanti, P.; Helfer, T.; Manfriani, C.; Uzielli, L.; Castelli, C.; Santacesaria, A.; Ricciardi, L.; Rossi, S.; Gril, J.; et al. Modelling of Hygro-Mechanical Behaviour of Wooden Panel Paintings: Model Calibration and Artworks Characterisation. *Herit. Sci.* **2024**, *12*, 5. [CrossRef]

[34] Califano, A.; Foti, P.; Baiesi, M.; Sepe, R.; Berto, F.; Bertolin, C. Machine Learning and Numerical Simulations for Predicting Critical Crack Conditions in Wooden Panels. *Int. J. Struct. Integr.* **2025**, *16*(4), 914–935. [CrossRef]

[35] Stöcklein, J.; Kaliske, M. Thermo-Hygro-Mechanically Coupled Modelling of Wood Including Two-Phase Moisture Diffusion for Transient Simulation of Wooden Structures at Mechanical and Climatic Loads. *Heat Mass Transf.* **2023**, *59*, 67–79. [CrossRef]

[36] Gagliardi, C.; Riparbelli, L.; Mazzanti, P.; Fioravanti, M. A Critical Review of Methods and Techniques Used for Monitoring Deformations in Wooden Panel Paintings. *Forests* **2025**, *16*(3), 546. [CrossRef]

[37] Grbovic, A.; Sedmak, A.; Petrovski, B.; Sghayer, A.; Sedmak, S.; Razavi, J.; Berto, F. Numerical Simulation of Fatigue Crack Growth in AA6156 T6 Panels. *Procedia Struct. Integr.* **2022**, *39*, 786–791. [CrossRef]

[38] Romanowicz, M.; Grygorczuk, M. Experimental Investigation of the Mode I Fracture Energy of Wood Using DIC and Secant Compliance Techniques and Its Numerical Validation. *Int. J. Solids Struct.* **2026**, *325*. [CrossRef]

Disclaimer/Publisher's Note: The views expressed in this article are those of the author(s) and do not necessarily reflect the views of the publisher or editors. The publisher and editors assume no responsibility for any injury or damage resulting from the use of information contained herein.

ACCEPTED